UC San Diego

UC San Diego Previously Published Works

Title

Ultraflexible electrodes for recording neural activity in the mouse spinal cord during motor behavior

Permalink

https://escholarship.org/uc/item/4s17534g

Journal

Cell Reports, 43(5)

ISSN

2639-1856

Authors

Wu, Yu

Temple, Benjamin A

Sevilla, Nicole

et al.

Publication Date

2024-05-01

DOI

10.1016/j.celrep.2024.114199

Copyright Information

This work is made available under the terms of a Creative Commons Attribution-NonCommercial-NoDerivatives License, available at https://creativecommons.org/licenses/by-nc-nd/4.0/

Peer reviewed

eScholarship.org Powered by the California Digital Library
University of California

Author Manuscript

Author Manuscript

Author Manuscript

Author Manuscript

HHS Public Access

Author manuscript

Cell Rep. Author manuscript; available in PMC 2024 July 09.

Published in final edited form as:

Cell Rep. 2024 May 28; 43(5): 114199. doi:10.1016/j.celrep.2024.114199.

Ultraflexible electrodes for recording neural activity in the mouse spinal cord during motor behavior

Yu Wu[1,2,8], **Benjamin A. Temple**[3,7,8], **Nicole Sevilla**[2,4], **Jiaao Zhang**[1,2], **Hanlin Zhu**[1,2], **Pavlo Zolotavin**[1,2], **Yifu Jin**[1,2], **Daniela Duarte**[5], **Elischa Sanders**[6], **Eiman Azim**[6], **Axel Nimmerjahn**[5], **Samuel L. Pfaff**[3,*], **Lan Luan**[1,2,4,*], **Chong Xie**[1,2,4,9,*]

[1]Department of Electrical and Computer Engineering, Rice University, Houston, TX 77005, USA

[2]Rice Neuroengineering Initiative, Rice University, Houston, TX 77030, USA

[3]Gene Expression Laboratory, Salk Institute for Biological Studies, La Jolla, CA 92037, USA

[4]Department of Bioengineering, Rice University, Houston, TX 77030, USA

[5]Waitt Advanced Biophotonics Center, Salk Institute for Biological Studies, La Jolla, CA 92037, USA

[6]Molecular Neurobiology Laboratory, Salk Institute for Biological Studies, La Jolla, CA 92037, USA

[7]Neurosciences Graduate Program, University of California, San Diego, La Jolla, CA 92037, USA

[8]These authors contributed equally

[9]Lead contact

SUMMARY

Implantable electrode arrays are powerful tools for directly interrogating neural circuitry in the brain, but implementing this technology in the spinal cord in behaving animals has been challenging due to the spinal cord's significant motion with respect to the vertebral column during behavior. Consequently, the individual and ensemble activity of spinal neurons processing motor commands remains poorly understood. Here, we demonstrate that custom ultraflexible 1-μm-thick polyimide nanoelectronic threads can conduct laminar recordings of many neuronal units within the lumbar spinal cord of unrestrained, freely moving mice. The extracellular action potentials

This is an open access article under the CC BY-NC-ND license (http://creativecommons.org/licenses/by-nc-nd/4.0/).

*Correspondence: pfaff@salk.edu (S.L.P.), lan.luan@rice.edu (L.L.), chong.xie@rice.edu (C.X.).

AUTHOR CONTRIBUTIONS

Conceptualization, C.X., L.L., S.L.P., Y.W., and B.A.T.; methodology – electrode design, C.X., Y.W., P.Z., and B.A.T.; methodology – surgical procedure, D.D., B.A.T., Y.W., N.S., and E.S., supervised by S.L.P., C.X., L.L., A.N., and E.A.; methodology – simulation, J.Z., supervised by C.X.; methodology – histology, B.A.T., Y.W., and Y.J., supervised by C.X., L.L., and S.L.P.; methodology – spike sorting and behavioral analysis, Y.W., J.Z., H.Z., N.S., and B.A.T., supervised by C.X. and L.L.; investigation, Y.W., B.A.T., J.Z., and N.S., supervised by C.X., L.L., and S.L.P.; writing – original draft, Y.W., L.L., and C.X.; writing – review & editing, L.L., C.X., S.L.P., Y.W., B.A.T., and N.S.; funding acquisition, C.X., L.L., S.L.P., A.N., and E.A.; resources, all authors; visualization, Y.W., N.S., and J.Z., supervised by C.X. and L.L.

SUPPLEMENTAL INFORMATION

Supplemental information can be found online at https://doi.org/10.1016/j.celrep.2024.114199.

DECLARATION OF INTERESTS

The authors declare no competing interests.

Author Manuscript Author Manuscript Author Manuscript Author Manuscript

have high signal-to-noise ratio, exhibit well-isolated feature clusters, and reveal diverse patterns of activity during locomotion. Furthermore, chronic recordings demonstrate the stable tracking of single units and their functional tuning over multiple days. This technology provides a path for elucidating how spinal circuits compute motor actions.

Graphical abstract

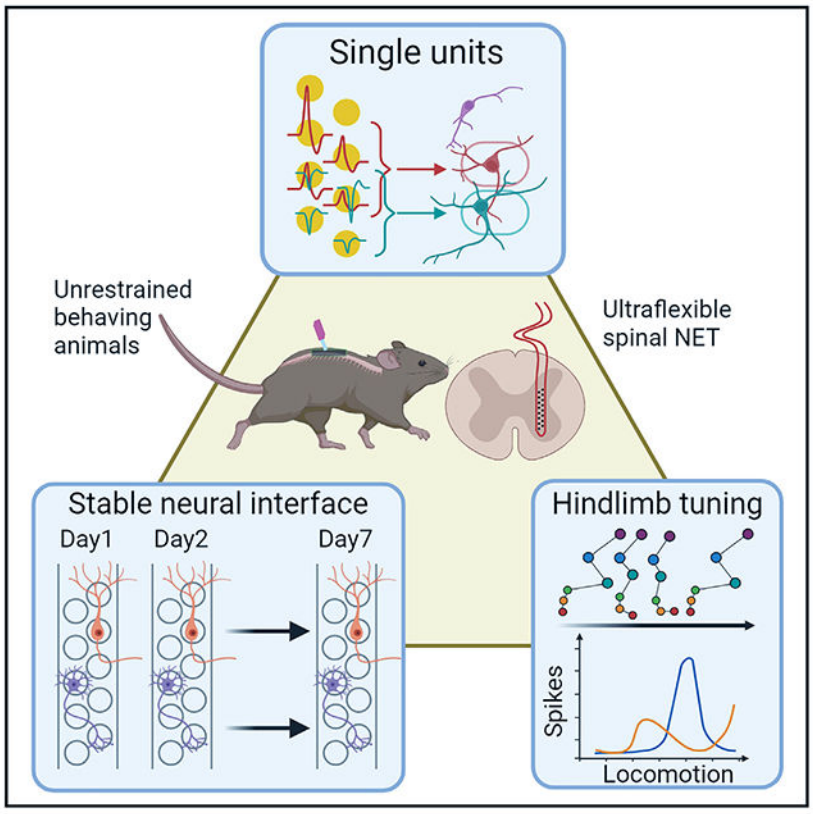

In brief

Wu et al. designed ultrathin flexible electrodes for intraspinal recording. The electrodes' flexibility yields a stable neural interface despite spinal cord motion. In unrestrained behaving mice, the well-isolated single units reveal diverse tuning to locomotion and allow for longitudinal tracking of neurons.

INTRODUCTION

Neurons within the spinal cord are instrumental in computing the output signals that drive vertebrate behavior by regulating muscle contractions, complex reflex circuits, pattern generators, propriospinal coordination between distant limbs, autonomic organs, sensory gains, and integrating and transmitting ascending signals.[1–3] The spinal neural networks linked to different motor outputs are comprised of intermingled cells with distinct physiological properties, and this neuronal diversity is reflected in the extreme molecular heterogeneity among spinal neurons.[4–9] Elegant genetic tools have been used in mice to

Author Manuscript Author Manuscript Author Manuscript Author Manuscript

trace connections and characterize the function of neuronal classes within the spinal cord, and these foundational studies have begun to reveal the underlying neural architecture for rhythmic stepping, coordination of flexion-extension, control of dexterous actions, inputs from higher brain regions, and feedback from different sensory modalities.[1,2,10–13] However, it remains unclear how the interconnected multicellular spinal circuits integrate and transform descending commands and sensory feedback into coherent outputs for precise and coordinated motor commands. A critical feature that is currently lacking is a thorough understanding of the firing relationships of neurons comprising the motor networks during unconstrained natural behavior in awake animals, especially mammals. Here, we sought to develop a method for recording the neuronal activity of ensembles of cells at the single unit level in the spinal cord of awake-behaving mice.

Population recordings of neurons have been achieved using calcium-sensitive fluorescent proteins (e.g., GCaMPs) and multi-electrode arrays. While each of these approaches has strengths, these technologies have been difficult to implement in the spinal cord of intact, behaving mice. Recent innovations have allowed for population recordings using GCaMPs in the mouse dorsal spinal cord.[14,15] However, these proxy events have time constants that are typically greater than 100 ms,[16] which do not accurately capture high-frequency spiking dynamics. In addition, myelinated axonal tracts surrounding the spinal gray matter typically limit optical access to all but sensory-related regions located in the superficial dorsal horn, currently precluding studies of motor circuit activity in the ventral horn of behaving mammals.[14]

While electrophysiological methods can, in principle, overcome the temporal and depth constraints of imaging, they face a significant obstacle presented by the motion of the spinal cord. The spinal tissue moves with an animal's body during behavior, exhibiting bending and displacement within the vertebrae. Because most electrodes are substantially more rigid than nervous tissue, they typically fail to stay compliant with the spinal cord during such motions, resulting in excessive noise, position drifts, injury to the tissue, and quick deterioration in recording performance.[17–20] As a result, electrophysiological recordings in the spinal cord are mostly restricted to *ex vivo*,[21,22] anesthetized,[23–26] or acute preparations.[27] Even in the impressive but few examples of spinal recordings in awake-behaving contexts, animals were highly constrained,[28–33] motor activity was tightly circumscribed (e.g., isometric contractions of wrist muscles),[28,29,31,32] and/or neurons were recorded one at a time[30,34,35] or for short time periods.[30,34] Importantly, because the spinal cord mediates whole-body motor behaviors, a deeper understanding of spinal circuits requires unrestrained recording during precisely those actions that drive the most severe displacements of tissue. Finally, the diverse and often longer time-scales relevant to spinal cord function present an additional challenge for intraspinal recording technologies. For example, open questions remain about the nature and extent of spinal plasticity in motor learning and recovery from injury, about the transition from acute to chronic pain, and about spinal responses to pharmacology.[36] Yet these questions are especially difficult to address, since they require a persistently intact interface between the recording device and spinal tissue.[17] Thus, limitations to conventional electrophysiology in the spinal cord impede functional studies to improve our understanding of the neural circuits underlying movement.

Author Manuscript Author Manuscript Author Manuscript Author Manuscript

Flexible electrodes have emerged as an effective solution for alleviating mechanical mismatch with tissue, but thus far their applications have been predominantly in the brain.[37] In previous studies, we engineered ultraflexible polymer electrodes, or nanoelectronic threads (NETs), with a total thickness of merely 1 μm, and demonstrated their efficacy in establishing an intact tissue-device interface and providing long-lasting, stable recordings of neuronal populations in the brain.[38,39] Here, we present a complete strategy including a custom ultraflexible probe and surgical implantation for single-unit recordings in the spinal cord of behaving mice. We designed and fabricated a 32-channel spinal NET to allow for targeting of the ventral spinal cord, where motor circuitry is located. We also developed surgical procedures for insertion of the NET into the lumbar cord, a region that drives hindlimb movement, by adapting a stabilization platform designed for imaging studies.[40,41] Using awake and freely running animals, we show that NETs recorded high signal-to-noise ratio (SNR) action potentials, enabling consistent isolation of single spinal units across motion states. These units display diverse spiking profiles and correlations with locomotion. Importantly, spinal NETs exhibited minimal electrode drift or adverse tissue impact, allowing for chronic studies of spinal activity. We show tracking of neuron populations across 7 days in locomoting mice and characterize the longitudinal tuning properties of single units. By enabling time-resolved, high-fidelity measurements of populations of single spinal neurons during natural behaviors, this technology will help drive fundamental advancements in the understanding of spinal cord neurophysiology.

RESULTS

Design, fabrication, and implantation of ultraflexible NETs to enable chronic electrophysiological recording in the mouse lumbar cord

The spinal cord often experiences significant displacement of dozens of micrometers during natural behaviors.[40] To mitigate mechanical mismatch and ensure faithful detection of individual neurons, electrodes must remain mechanically compliant with these movements. Therefore, to inform the design of the electrode, particularly its thickness, we used finite element modeling to evaluate the strain energy in the spinal tissue surrounding rigid silicon[42,43] and tungsten microwire electrodes,[44–46] as well as polymer (polyimide) electrodes of various thicknesses (Figures 1A and S1A). We simulated representative strains in the mouse spinal cord during motor activities by applying a combination of displacements and stretching (as informed from imaging literature) to a 5-mm segment of spinal tissue.[40] To mimic the natural movements of the spinal cord, we modeled displacements of 150 and 250 mm at the two terminals of neural tissue along the rostral-caudal direction, and an additional displacement of 50 μm along the medial-lateral direction (Figure 1A, details of simulation specified in STAR Methods). For polyimide probes, the strain energy scales super-linearly with thickness (Figure 1B). Specifically, polyimide devices of 1-μm thickness can substantially reduce the strain energy density (5.84×10^{-5} mJ/mm^3) at the probe-tissue interface by ~142 times from silicon (4.11×10^{-3} mJ/mm^3), ~245 times from tungsten (1.43×10^{-2} mJ/mm^3), and ~25 times from 15-μm polyimide (1.46×10^{-3} mJ/mm^3) (Figure 1B). Notably, the modeled strain energy induced by a 1-μm-thickness polyimide implant is comparable with the naturally occurring strain energy in the spinal tissue (1.75×10^{-5} mJ/mm^3).

Author Manuscript Author Manuscript Author Manuscript Author Manuscript

In an empirical complement to this model, we evaluated the spinal tissue response to chronic implantation of a standard rigid silicon probe (28 days post implantation, probe cross-section: 23 × 85 μm), and observed significant glial scarring (Figure 1A, right). By contrast, later in this paper we evaluated the response to a 1-μm-thick polyimide probe, which exhibits minimal impact on surrounding tissue. Together, these findings indicated that 1-μm-thick ultrathin NETs, similar to those we have developed and demonstrated in the brain, could effectively eliminate the mechanical mismatch at the electrode-tissue interface in the highly mobile spinal cord.

We designed and microfabricated a 32-channel NET tailored to the anatomy of the mouse spinal cord (Figures 1C–1G). We placed our recording area across a length of 600 μm to sample across the ventral spinal cord, where motor circuits are situated. To strike a balance between depth coverage and contact density, which improves the isolation of individual units,[37] we arranged recording contacts with a diameter of 25 μm in a two-row, zigzag pattern (Figure 1C). To further minimize the footprint of the implant, we implemented a tapered width of 122–65 μm. Finally, although separately implanted rigid reference electrodes are conventionally used in brain recordings, they are inappropriate in the spinal cord since their large and stiff character is prone to causing motion-related tissue damage. Thus, we positioned local reference contacts directly above the recording contacts (Figure 1C, right). Post-microfabrication profilometry confirmed that these probes had an overall thickness of 1.1 μm as designed (Figure 1D), thus exhibiting the desired ultraflexibility (Figure 1E). The flexible section had a total length of 7 mm, which includes the insertion depth, routing distance, and necessary redundancy critical to accommodate motions, as elaborated on later.

Through iterative implantation testing we identified that minimal surgical footprint and slow implantation speed were important factors for achieving high-quality recording. Therefore, we adopted a “microneedle-thread strategy,”[39] wherein the NET, with a micro-hole at the distal end, was threaded to a 50-μm-diameter microneedle with a micromachined tip (Figure 1F). During implantation, the needle pushed the NET into the tissue at a slow speed (approximately 10 μm/s) that minimized tissue insult.[47] The implantation location was chosen to be 50–250 μm lateral from the dorsal spinal vein and approximately 1,000-μm deep in tissue segment L2, ensuring that most of the contacts would record from the ventral gray matter (Figures 1G and S1B). Once NETs reached the designated depth, the needle was retracted, releasing the NET in the tissue (Figure 1H, see Figure S1D for the insertion procedure).

Equally important as a tissue-compliant probe for high-quality spinal recording is a strategy for securing the recording backstage. We modified a chronic imaging chamber of the mouse spinal cord[40,41] to provide a mount for the probe’s backend electronics adjacent to the implantation site (Figures 1I and S1C, see details in STAR Methods). The spinal platform consisted of two metal bars that were clamped onto the vertebrae, alongside a top plate that was secured onto the bars and held a glass window (Figure 1I). The NET was implanted into the spinal tissue beneath the window and routed outside of the window for connections with external electronics (Figures 1I and S1E). Importantly, we found it critical to incorporate a flexible segment of NET between the implantation site and the fixation point near the metal

Author Manuscript Author Manuscript Author Manuscript Author Manuscript

plate during surgery. Thereby, we implemented a gap filled with saline between the dorsal surface and glass window, where the flexible thread can move freely during motions (Figure S1E). The thickness of the gap was approximately 300–500 μm. The window was fixed with the backstage, and therefore there is no extra stress to the electrode or the spinal cord. This flexible section accommodates micromotions of the spinal cord when the animals are in motion (Figure S1E; Video S1), without subjecting the implantation section of the NET to excessive stress. This approach allows for reliable chronic connection to the electrodes while minimizing disruptions to recordings from the animal's movements. It also minimizes disruptions to the animal's movements from the presence of the probe. Implanted animals exhibited normal motor behaviors, including activities such as whisking, rearing, digging, walking, exploring, scratching, grooming, and bipedal standing (Figure 1J; Videos S2 and S3). The results obtained from these experiments are presented in the subsequent sections.

Well-isolated single-unit activity in awake, unrestrained mice

Accurate detection of single-unit activity is critical for understanding the function of individual neurons within diverse populations. This requires both close proximity between electrodes and neurons as well as a stable tissue-electrode interface, as the detection range is limited (<50 μm)[37] and thus even small changes of the probe-neuron distance can result in inaccurate single-unit isolation. First, we examined the single-unit recording quality of NETs in the spinal cord of animals moving freely without restraint. Figure 2A shows a snapshot of a representative recording session (band-pass filtered), in which 31 out of 32 channels spanning a vertical range of 600 μm in the lumbar segment recorded evident spikes. After spike sorting using a standard algorithm, MountainSort, followed by manual curation with a set of structured criteria,[48] we isolated 31 single units from this representative session, providing a yield of 1 single unit per channel (see STAR Methods for sorting details).

We designed the spinal NET to have high contact density, allowing each contact to capture multiple waveforms and each waveform to span over multiple contacts (Figure 2B). This poly-trode characteristic enhances single-unit sorting fidelity.[49] To examine the quality of single unit isolation, we evaluated each unit's (1) waveform and peak-to-peak amplitude (Figure 2C), (2) inter-spike interval (ISI) (Figures 2C and S2A), (3) amplitude distribution (Figure 2C), and (4) the firing auto-correlogram (ACG) and cross-correlograms to other units (Figure 2D and S2B).[50] All these metrics indicate little contamination from multi-unit activity in the isolated single units. Moreover, to provide additional evidence of distinct isolated units in a manner independent of our conventional spike sorting in MountainSort, we employed Uniform Manifold Approximation and Projection (UMAP) analysis to a group of channels to reduce the recording feature dimensions. We focused on a region of channels (dashed rectangles in Figures 2B and 2E) with the highest amount of neural activity because densely overlapping activity of multiple signal sources presents the greatest challenge to effective single unit isolation. We observed clearly separated clusters: the yield was 12 single units from 8 channels, which matched with the units sorted by MountainSort from the same 8 channels (Figure 2D, UMAP clouds). Clusters identified in the UMAP are further confirmed to be independent of each other by inspection of their cross-correlograms (Figure 2D). Finally, by triangulation of detected waveforms, we estimated the locations of each

Author Manuscript Author Manuscript Author Manuscript Author Manuscript

sorted unit with respect to the contacts and provided a snapshot of the populational activity including firing rates, amplitudes, and locations along depth (Figure 2E).

In $n = 12$ animals, NETs were consistently able to record high SNR action potentials that resulted in well-isolated single units when the animals were freely roaming in their home cages. Taking all animals' example recording sessions together, we sorted 561 total units with a single-unit yield per channel at 0.73, SNR of 12.15 ± 3.03 (mean ± SD, Figure 2F), and unit isolation score of 0.95 ± 0.10 (mean ± SD, Figure 2G). Having recorded hundreds of single units allowed us to investigate spinal waveform features and their population distribution, which provides insights into the range of biophysical properties across the cells we sampled.[51] We found wide distributions of the three key features (Figures 2H–2K): the rise time of the auto-correlogram, trough-to-peak periods, and average firing rate. Notably, one neuron in a single recording session can reach a firing rate as high as 99 Hz. The trough-to-peak periods have a tri-modal distribution where most values were <0.45 ms. These distributions suggest the presence of diverse cell types in the recorded population (see discussion).

Robust single-unit recording during locomotion reveals functional tuning of individual neurons

To interpret the function of cells in spinal circuits, it is critical to monitor the activity of individual neurons across various behavioral states. However, motion-induced noise and drift at the electrode-tissue interface can undermine the reliability and consistency of recordings and sorting.[52] To address whether our recording approach covered this technological gap, we investigated whether NETs could maintain high-SNR recordings during vigorous movements and, more demandingly, minimize changes in detected spike features to allow continuous identification of the same units throughout recording sessions that had varying motion intensities ($n = 4$ animals).

We first subjected the animals implanted with NETs in the L2 segment to a self-motivated motion pattern in which the animal intermittently walked and stood still on a motorized treadmill. Figure 3A provides a snapshot of the recording from all channels in one animal. Remarkably, as the animal transitioned between moving and standing states, NETs consistently recorded spiking activities and field potentials across all functioning channels with minimal observable interruption (Video S4, example recording of a single channel is shown in Figures 3B and 3C). Importantly, we successfully isolated the same single units across moving and standing episodes despite the animal's continuously changing motion states. All 26 sorted single units had one-to-one matching across conditions, indicating that there were no lost or added units induced artificially by the animal changing motion (Figure 3A). These units had nearly identical unit waveforms between moving and standing states, despite the obvious alterations in the temporal pattern of spiking (Figure 3B) and local field potential (Figure 3C). Furthermore, we calculated the pairwise correlation among all units' waveforms and demonstrated that waveforms of the same units exhibited high similarity between moving and standing conditions, whereas waveforms of different units differed significantly irrespective of behavior states (Figure 3D within-unit and cross-unit

Author Manuscript Author Manuscript Author Manuscript Author Manuscript

distributions, two-sided Wilcoxon rank-sum test, $p = 4.7e{-}18$). These results suggest that NETs offer stable recordings to monitor the same single units in varying motion states.

We next sought to evaluate whether the probe could be used to measure the functional tuning of individual lumbar neurons during a motor behavior, locomotion, which is significantly controlled by spinal circuits.[53] We captured videos of the animal's locomotion (n = 4 animals) while simultaneously recording spinal neurons. Using the video annotation software DeepLabCut,[54] we labeled and analyzed the movements of six hindlimb joints (iliac crest, hip, knee, ankle, metatarsophalangeal, and toe) from a side view ipsilateral to the probe implantation (Figures 3E–3G, S3A, and S3B), as well as the two-paw gait from the bottom view (Figure S3C). Locomotion is a rhythmic behavior—a low-frequency oscillation of the limbs. Thus, to evaluate the nature and extent of unit correlations with motor output, we employed frequency-domain analyses[55–57] to report the magnitude and phase of unit coherence with the underlying locomotor rhythm. In a representative recording, 15/32 units exhibit significant coherence with the locomotor frequency of 2 Hz while others do not (Figure 3F).

Provided the clear and diverse correlations between unit activity and locomotion, we then explored the nature of these relationships in more granular detail (Figures 3G, S3, and S4). First, all recorded units, at the population level (total firing rate), exhibited clear modulation by the on/off states of locomotion (multi-step walking vs. standing) (Figure S4). At finer timescale (several oscillatory cycles of joint angle), we draw attention to two distinct, simultaneously recorded neurons that both have significant coherence to the underlying locomotor rhythm but are tuned to different features of the locomotor cycle. While a first unit exhibited bursting firing and is locked to the rising edge of the knee angle (Figure 3G, unit 1 with red color), a second unit has a more persistent firing character (Figure 3G, unit 2 with blue color). Other illustrative examples are: a unit whose firing rate raised at the peaks of ankle angle (Figure S3A, 12 dpi), a unit that fired sparsely but only at the valley of hip angle (Figure S3B, 7 dpi), and a unit that showed phase-locking with the hind paw position (Figure S3D, 6 dpi). These single units were cleanly isolated, as signified in their distinctive waveforms and functional tuning, ISI histograms, and cross-correlograms (Figures 3G, S3A, S3B, S3E–S3I). It is important to note that, in addition to rhythmic units of diverse character, we also recorded well-isolated units that did not display obvious correlation to locomotion (see Figure S3I for examples). The diversity of rhythmic tuning and the presence of well-isolated but nonrhythmic units provides further evidence that the strong single-unit correlations we detected did not stem merely from motion artifacts. These results therefore not only verified NETs' stable recordings during vigorous motor behavior, but also provided a glimpse of the complexity of spinal neural function.

Multiple-day recording stability in task-performing animals

Longitudinal spinal electrophysiology studies to investigate phenomena such as motor learning and recovery from injury would require repeated measurements over chronic intervals. Therefore, given the stability we observed at shorter timescales, we also asked: can NETs effectively record spinal neurons over extended periods, and can they track the same neurons?

Author Manuscript Author Manuscript Author Manuscript Author Manuscript

While it is difficult to establish definitively that single units are being tracked over long time intervals, we present a range of evidence—stable detected location, stable biophysical properties (e.g., ISI distribution and waveform), and stable relationship with respect to the behavioral markers—that indicates tracking of putative stable units across days. We performed electrophysiology recordings for 7 consecutive days. During each daily session, we captured neural activity while the animals ran on the treadmill (n = 2 animals). Figure 4 shows the 7-day recordings from one animal (days 60–66 post implantation). To evaluate recording stability and quantify potential electrode drift, we first sorted all sessions independently and estimated cluster positions with respect to contacts using triangulation of detected waveforms (Figure 4A).[58,59] Next, to determine whether we could link unit clusters in neighboring sessions, we employed a conventional tracking approach and identified each unit's mutual nearest neighbor (MNN)[60] (see STAR Methods). This required that each putatively linked unit was more similar to itself than to any other unit across recordings. From day 1 to day 2, a total of 25 unit pairs had the most similarity to each other in both waveform and location, which we identified as putative same neurons (Figure 4A, pairs are color coded). Extending the same method to 7 consecutive days, we tracked a total of 16 units that consistently displayed similar waveforms and locations across all 7 days (Figure 4B). We then analyzed daily drift from unit positions for all tracked units across the 7-day duration, and we found that 90% of the drifting distances were within ±13 μm (Figure 4C), which is less than the spacing between neighboring recording contacts.

To assess the performance of the MNN algorithm by independent means, we calculated the Euclidean distances of concatenated waveforms (stitched waveforms from all 32 channels) of all cluster pairs (STAR Methods). In Figure 4D, the distances of linked clusters to all other clusters (n = 2,880) were normalized to the distances of linked clusters (n = 96), which was marked as unity. Remarkably, 99% unmatched pairs had Euclidean distances from each other greater than 3.8 times those of the matched pairs, confirming that matched pairs were considerably more similar to themselves than to any other recorded unit. This is close to an earlier established benchmark of 2.6 times unity to validate MNN in cortex,[60] thereby further suggesting that our approach of tracking units based on waveform similarities across daily sessions performed well from the perspective of previously established standards.

To provide an additional layer of scrutiny to our tracking approach, we also examined the stability of unit waveforms, amplitudes, and ISI distributions from the first to the last day. As depicted in Figure 4E, the 16 trackable units exhibited consistent waveforms on the primary channels over multiple days. This consistency is also evident in the average amplitudes of three exemplary units and their corresponding ISI histograms (Figures 4F and 4G, also see Figure S5A for ISIs of all trackable units). It is worth noting that another animal showed fewer units that could be continuously tracked shortly after implantation (Figure S5B, days 10–16 post implantation), indicating that neuron-probe interface might still undergo a dynamic recovery phase in the early stages following implantation.[38]

While it would be circular to conclude from the observation of stable tuning properties that the same unit is being tracked over time (since this inference depends on secure tracking in the first place), the evidence above indicating successful tracking over days allowed us to ask whether any of these putative stable single units exhibited longitudinal functional

Author Manuscript Author Manuscript Author Manuscript Author Manuscript

tuning with respect to behavioral markers. Figure 4H shows the dependence of firing rate on the knee angular velocity and on the ankle angle for two representative units, respectively (also see Figure S5C for the tuning curves of all trackable units). The first unit displayed remarkable tuning stability in the firing rate vs. knee angular velocities over the entire time course. The second unit's daily tuning had moderate variations in the absolute values of firing rate, but the tuning angles and the overall dependence of the firing rate on the ankle angle remained consistent across 7 days. Normalizing the firing rate further shows the tuning consistency across days (Figure S5D). Together, these results indicate the promise of NETs for future spinal studies that require longitudinal measures.

Chronic performance and neural interface

Longitudinal studies require clear expectations of changes in recording quality over time. Here, to evaluate the chronic performance of the spinal NET, we performed longitudinal recordings post implantation and postmortem histological studies.

We found that the intraspinal recordings had relatively high efficacy in the first 10 days post implantation in a cohort of animals for this chronic study ($n = 8$ animals). The average unit yield per channel was 1.17 ± 0.10 (mean ± SE) on day 1, and at 0.69 ± 0.13 (mean ± SE) by day 10 post implantation (Figure 5A). Furthermore, 50% of the animals (four out of eight mice) had long-lasting recordings, with unit yield stabilized around 0.5 after at least 1 month post implantation (Figure 5B). In these animals, electrode impedance slowly increased over a period of a month to 2 MΩ and then remained stable thereafter (Figure 5C). Notably, our longest implantation lasted for over 5 months with sortable spikes (Figure 5D).

Given that the changes in most electrophysiological recordings subsided at 1 month post implantation, we conducted histological analysis after this time point ($n = 3$ mice). In contrast with the marked reaction observed after chronic (28 days) spinal implantation of a rigid silicon probe (Figure 1A), after the same time course we found a relatively intact tissue-NET interface, including the absence of scar tissues, low level of microglia (visualized by antibody against Iba1) and astrocyte (antibody against glial fibrillary acidic protein) activation, and no observable neuronal degeneration in the areas surrounding NETs (Figure 5E). Quantitative analysis of the spatial distribution of cells near the implantation site showed slight increase in microglia and astrocyte density near the electrodes but no decrease in neuronal density along either rostral-caudal or medial-lateral directions (Figure 5F). Statistically, we found no significant difference in neuron and astrocyte density between near-probe and far-away locations, while microglia density showed marginally significant difference (Figure S6, ns for neuron and astrocyte, $p = 0.0483$ for microglia). These results indicate that NETs can establish a chronically functioning interface with the spinal cord, but at the same time the longevity of recordings varied across animals, highlighting the systematic challenges associated with achieving long-lasting intraspinal recording of high-quality single units.

DISCUSSION

Electrophysiology, when paired with behavioral measurements, offers a powerful approach to directly investigate neuronal and circuit functions. However, a major challenge of

Author Manuscript Author Manuscript Author Manuscript Author Manuscript

this method is maintaining the proximity of electrodes to individual neurons. Implanted electrodes typically record action potentials from immediately nearby neurons (<~50 μm).[61] Even small displacements between the recording contacts and the cells lead to waveform changes[62] or signal loss. Furthermore, delicate nervous tissues are sensitive to micromotion-induced injuries. Although it has become routine for scientists to record neurons in different brain regions in awake behaving animals, excessive electrode-tissue displacements in the spinal cord prevent the same functional electrophysiological methods from being effective. This technical challenge has significantly constrained our comprehension of the spinal cord. In this work, intraspinal NETs were able to record from spinal neurons in action, revealing that the activity of spinal interneurons is highly heterogeneous at multiple levels: firing, biophysical properties (Figure 2H–2K), and tuning and spatial position with respect to the locomotor rhythm (Figure 3F–3G, S3A, S3B, and S3I). Furthermore, the stable recording by NET allowed us to investigate the day-to-day tuning stability of spinal neurons (Figure 4H and S5C), indicating the existence of spinal units with consistent tuning across days.

Probe design and implantation strategy

We chose to use a mouse model because of the abundance of genetic and imaging methods available for mice. This technical study therefore can serve as the foundation for future studies that work in tandem with these tools, as we have demonstrated in the brain.[63–65] Meanwhile, the small size of the mouse spinal cord also imposed challenges for probe design and mechanical stability after implantation. In each spinal cord segment, many neurons responsible for critical motor and sensory functions are packed in a small volume, making it sensitive to mild disruptions of the tissue. For example, we observed loss of motor functions 1 week after the implantation of a typical reference electrode commonly used in the brain (Ag or stainless-steel wires of 75 μm in diameter). We addressed this issue by integrating the reference electrode into the flexible NET thread, which completely avoided the use of rigid materials in neural tissue.

In addition, the small surface area and fragile nature of the mouse vertebrae make it difficult to securely mount backend electronics. Although the NET is designed to accommodate micrometer-scale tissue displacement, it cannot withstand larger millimeter-scale dislocations off the vertebrae. Therefore, to provide a stable base for the probe and its recording backstage, we adopted previously reported chronic imaging platforms, which are capable of accommodating the comparatively larger weight and torque from wearable microscopes and comfortably exceed the requirement of our recording approach.[15,40]

In this study, we did not pursue precise targeting in medial-lateral directions during implantation. Instead, our priority was to avoid vasculature damage, and therefore the dorsal entry sites (among animals) landed in the range of 50–250 μm from midline. This strategy could result in coverage variations in gray matter and white matter and needs to be taken into consideration in future study design.

Well-isolated single units reveal neuron properties

In this study, we prioritized single unit isolation by using a dense contact pattern. A direct benefit of this design is improved efficacy in cell property classification based on

Author Manuscript Author Manuscript Author Manuscript Author Manuscript

unit features, such as waveform trough-to-peak and bursting pattern. Notably, the use of awake behaving recordings is crucial in studying these cell-type-specific features, as neuronal response properties can be shaped not just by anesthesia but also by restraint of the animal.[66,67] Here, NETs provide an opportunity to observe the highly diverse features of spinal neurons. The trough-to-peak of unit waveforms range from 0.12 to 0.45 ms, containing mostly narrow-waveform units (<0.45 ms).[51] The ACG rise times range from 0.10 to 44.80 ms, indicating the existence of both bursting and non-bursting units. Average firing rates range from 0.03 to 99.02 Hz, suggesting there were both frequent-firing and sparse-firing units. Although these features alone are far from sufficient to establish cell types, they demonstrated that the spinal cord is a highly diverse system.

Diverse neural activities tuned to locomotion

A major fruitful research program has focused on the developmental and genetic features of the spinal cord.[1,2,68] For example, a framework has emerged in which spinal cord neurons can be divided into cell types, known as the cardinal classes, based on their origin in distinct neural progenitor domains.[9] Within these classes, there is increasing evidence of even further transcriptional and projection-target diversity.[69] However, previous attempts to understand the functions of these cell types have largely been limited to anatomical and silencing experiments.[70] Here, we demonstrate an approach to correlate the electrical spiking patterns of multiple simultaneously recorded neurons with locomotion in awake and task-performing mice. We observed that motion-correlated units also exhibited remarkably diverse firing patterns (including non-rhythmic spiking even during rhythmic behaviors) and waveform characteristics. In light of the significant genetic diversity discovered in the spinal cord, our technique opens the door to future recording studies that might connect genetic signatures to electrophysiological profiles to integrate these aspects of our understanding of spinal circuits.

We targeted our electrodes to the intermediate layers of the spinal cord, where most cells are local circuit neurons (interneurons). These cells sit at least one synapse away from the motor neurons. Among them, some also integrate sensory feedback with descending motor commands. This leaves their role in motor coding potentially more complicated than the one-to-one unit-to-muscle relationships exhibited by motor neurons. Thus, the firing of these neurons may not in all cases be coherently modulated by motor activity at fine timescales.

Longitudinal stability

Longevity and stability are important merits of any recording modality, and they are particularly challenging to achieve in the spinal cord because of its frequent and large motions, which can lead to signal loss, corruption, or drift.[62] Furthermore, mechanical mismatch at the recording-tissue interface can elicit inflammatory reactions and neuronal degeneration, both of which can result not only in signal loss but also injury to the spinal circuits that an investigator is trying to observe. Here, our spinal NET provides the remarkable ability to maintain high-quality recordings and track the same units from task-performing mice for at least 7 days. The ability to record from the same neuronal population has the additional benefit of improving statistical sampling and reducing the animal number required in a study.[60,71,72] Importantly, this capability also introduces the

Author Manuscript Author Manuscript Author Manuscript Author Manuscript

possibility for a great range of experiments in spinal physiology by enabling investigation of cell-specific functions underlying chronic events, such as chronic pain and learning-related plasticity. For studies that require stable recordings across days, we recommend closely monitoring the day-to-day unit yield and the consistency of unit waveform and location to determine the starting time of unit tracking.

Limitations of the study

Despite the promising results, the overall recording outcome in this study was nonetheless relatively inferior to those in the brain using similar electrodes.[65,73] One notable issue was the observed degradation of unit yield over time in almost all the animals. Only about half of animals (four out of eight) had long-lasting recordings over several months, while the other half had no detectable single units after 2–3 weeks post implantation. In addition, although NETs significantly mitigated the risk of chronic tissue damage and immune reactions compared with rigid electrodes, adverse tissue response and its potential impact on neurophysiology remains an important consideration for any invasive method. In our procedures, we acknowledge key contributing factors to detectable tissue injury and compromised recording, including (1) tissue dimpling caused by inserting the electrode, (2) non-axial motions of the tungsten needle during insertion and retraction, (3) incomplete seal of the glass window, and (4) unstable mounting of the backstage. These issues occurred in pilot tests while we were optimizing surgical techniques and were avoided for animals reported in this study. Moreover, significant motion of the cord, which is known to be much greater than brain tissue, likely played a role in signal degradation, but a separate focused investigation is necessary to optimize this technology for long-lasting recording exceeding a few weeks. Another limitation of our current spinal NETs is that, while they make a scientific advance by recording from multiple spinal neurons at the same time, they have only 32 contacts each, a limitation imposed by the conventional backstage electronics that we employed in this study. This paper provides the proof-of-principle for the NET spinal recording approach, which can be adapted in the future for custom lead-out electronics that enable higher channel count without increasing the probe width (e.g., using Ebeam lithography[73]). While the spinal NETs of the current study provide a sizable coverage concentrated on the ventral cord, higher channel count and the ability to implant at multiple sites simultaneously are desirable features to allow for improved deciphering of spinal function. As recent studies using NET electrodes in the brain have established, the small footprint of these probes makes them easily scalable for implantations of multiple shanks that enable higher channel counts.[65] Finally, we note that, although this study focused on implantations in the lumbar region, future studies could explore other spinal segments, where circuits contributing to the control of diverse behaviors such as reaching (cervical), micturition (sacral), and autonomic-control (thoracic) reside.

A tool for future spinal cord research

The development of the spinal NET has been a collaborative effort involving an iterative design and validation process between engineering and biology groups. The high-density ultraflexible spinal electrode presented in this paper provides a powerful tool that will allow researchers to ask and answer questions about neural function in the spinal cord, such as

Author Manuscript Author Manuscript Author Manuscript Author Manuscript

etiology and progression of spinal cord injury and disease, intraspinal interfaces that treat spinal cord injury, stroke, movement disorders, and motor neuron diseases.

STAR★METHODS

RESOURCE AVAILABILITY

Lead contact—Further information and requests for resources and reagents should be directed to and will be fulfilled by the lead contact, Chong Xie (chong.xie@rice.edu).

Materials availability—This study did not generate new animal lines or unique reagents.

Data and code availability—All data reported in this paper will be shared by the lead contact upon request.

All original code has been deposited at Zenodo and is publicly available as of the date of publication. DOIs are listed in the Key resources table.

Any additional information required to reanalyze the data reported in this paper is available from the lead contact upon request.

EXPERIMENTAL MODEL AND STUDY PARTICIPANT DETAILS

Animals—A total of $n = 15$ mice (7 male, 8 female) at least 8 weeks of age or older (C57BL/6J) were bred on-site from breeding pairs acquired from Jackson Laboratories (Bar Harbor, ME). Mice were single housed following implantation of NETs in the Animal Resource facility at Rice University and Salk Institute. All surgical and experimental procedures were approved by the Institutional Animal Care and Use Committee (IACUC) at Rice University and Salk Institute and comply with the National Institutes of Health guide for the care and use of Laboratory animals.

METHOD DETAILS

Simulation of strain energy in moving spinal cord tissue—We built finite element models using Ansys Mechanical APDL software (Ansys) to simulate the situation where the spinal cord tissue moves against the implanted probe. Following the specifications from Ref[74], only the linear properties (Poisson's ratio and Young's modulus) are considered in the simulation (see table below):

Material properties used for simulation

	Neural tissue	Tungsten	Silicon	Polyimide
Poisson's ratio	0.45	0.28	0.278	0.34
Young's Modulus (MPa)	0.0954	400000	142000	2760

The length of the cord is set to 5mm with 1.2 mm in height and 2mm in width. The cross-sectional shape of spinal cord was adopted from Ref[74]. We modeled three types of probes that are commonly used for *in vivo* neural recordings: (i) rigid Si probe of 85 μm

Author Manuscript Author Manuscript Author Manuscript Author Manuscript

in width, 23 μm in thickness, and 2100-μm long; (ii) rigid tungsten wire probe of 30-μm diameter and 2100-μm long; (iii) flexible PI probes of 100 μm in width, 2613 μm in length, and thickness ranging from 1 μm to 15 μm; The insertion depth is set as 1000 μm for all simulations. For the PI probes, we initially set the bottom 1200 μm of the shank as straight and the top 1413 μm as a 90-degree arc of 900μm radius. This is to simulate the initial redundant length of the flexible shank after implantation.

To simulate the relative movement between tissue and probe, we fixed the top end of the shank with zero displacement, meanwhile we displaced one end of the spinal cord by 150 μm and the other end by 250 μm in the rostral-caudal direction. The tissue was also displaced by 50 μm in medial-lateral direction. We followed measurements from previous *in vivo* imaging for these displacement values so that our model resembled tissue movements during natural activity.[40] The output of simulation returns the strain energy gained by each mesh volume, which is defined as the elastic potential energy during deformation under force. The strain energy density of each mesh is then calculated as:

$$StrainEnergyDensity = \frac{StrainEnergy}{V_{mesh}}$$

where V_{mesh} is the volume of a single mesh. The strain energy density was averaged from a $200\ \mu m \times 200\ \mu m \times 140\ \mu m$ cubic volume of tissue surrounding the implanted probes.

It should be noted that the inserted portions of the probes were treated as mechanically fixed with neural tissue. This is realistic for small displacements (tens of microns scale) which are relevant in this study. For greater displacements (e.g., mm scale), however, slipping motions need to be considered.

NET probe fabrication and assembly—Given the impact of electrode dimension on neural interface, we chose ultrathin non-stretchable polyimide to prioritize minimizing the probe dimensions over stretchability. Electrode layout of spinal NET went through three iterative designs. The first iteration had an electrode contact dimension of $40 \times 40\ \mu m$ squares and no integrated reference, which could not effectively resolve single units and caused excessive tissue damage from the need for a rigid reference electrode. The second iteration had smaller round contacts of 15 μm diameter in a “tetrode” pattern of diamond-shaped four-contact clusters, which acquired better-isolated units but also did not have an integrated reference. The third iteration addressed these two issues as described in Results. We followed our previously reported procedure for fabricating NET electrodes,[38] except using PI as dielectric material, and sputtered IrOx as electrode material. Metal stack of Cr (5 nm) – Au (80 nm) – Cr (5 nm) was used for the connective tracks using photolithography and Ebeam evaporation. 112 NETs can be fabricated on a 4-inch wafer, among which 90–100 do not show trace line breaks based on optical inspection. Detailed procedures for NET probe assembly can be found in.[75] After fabrication, the NET was electrically bonded to the PCB connector through ball grid array (BGA), and epoxy was applied to mechanically reinforce the bonding. To fabricate the tungsten needle, a 50-μm tungsten wire was electrochemically etched in 0.8 M KOH solution to produce the anchor post (10–20 μm in diameter, 100–150 μm in length). Then a restrictive tubing (26 G stainless steel)

Author Manuscript Author Manuscript Author Manuscript Author Manuscript

along with the tungsten needle was fixed on NET's glass substrate by epoxy. In the end, the flexible shank was released from the glass substrate by Ni etchant (Nickel Etchant Type I, Transene), and then threaded onto the anchor post through manual manipulation. Before surgery, the assembled probe was dipped in PBS for impedance measurement, and probes with more than 25 functional electrodes (impedance <700 kΩ) were used in implantation.

Surgical procedure—We followed the reported procedures to implant chronic imaging chamber.[40,76] Briefly, mice were anesthetized with either 1.5%–2% isoflurane or a three part cocktail of Fentanyl (0.05 mg/kg), Midazolam Hydrochloride (5 mg/kg), and Dexmedetomidin Hydrochloride (0.5 mg/kg), shaved along their back using clippers and then placed on a heating pad with temperature controlled by rectal probe feedback for the duration of the surgery. The area of the skin around the incision site was disinfected by 70% ethanol, followed by betadine using cotton swabs. A longitudinal incision (1 cm–1.5 cm long) of the skin along the back was made over the L1-L3 lumbar segments and retracted laterally. Musculature overlying T11-T12 vertebrae was removed from the dorsal laminae, dorsal spinous processes and the articular processes using Dumont forceps and micro scissors. Lateral and dorsal bone surfaces of the spinal column were cleaned using a curette to create 9 mm of bone surface for the fitting of a metal chamber to the lateral edges of L1-L3. The chamber implant consists of: i) two small sidebars measuring 9 mm × 2 mm that are pressed against the spine; and ii) a metal top plate (10 mm × 10 mm) that locks the sidebars through miniature screws. After implanting the metal chamber, a laminectomy on L2 was performed using micro scissors to expose the spinal cord neural tissue for NET insertion.

Following the laminectomy that created an opening to expose the spinal tissue, the tungsten needle, carrying the ultraflexible shank, was inserted into the neural tissue at ~10 μm/s, and then pulled out from tissue manually. During our procedure development, the most common failure mode for implanting the NETs was the flexible thread being pulled out from neural tissue during needle retraction. This risk was substantially mitigated by following several guidelines: 1) after insertion, we thoroughly rinsed the needle/thread assembly with saline to create a lubricative liquid layer between the needle and thread, thus reducing friction, 2) we manually retracted the needle at high acceleration and speed, and 3) we reduced tissue dimpling by making a small incision on the dura before insertion. A custom-cut glass window (#0 or #1 coverslips) was then placed on top of the laminectomy opening, and PBS was used to fill the space underneath. The opening was further sealed by tissue adhesive to the edges of the window, and then adhesive cement (C&B-Metabond, Parkell) all over the silicone. The PCB connector was fixed onto the metal top plate through the adhesive cement (C&B-Metabond, Parkell) and reinforced by a titanium plate (custom cut to the diameter of the PCB connector). To close the tissue, the surrounding skin was glued around the edge of the imaging chamber using tissue adhesive (Vetbond tissue adhesive, 3M). Note that although we tried to target interneurons and motorneurons during implantation, we often needed to compromise precision in order to avoid hitting vasculatures, which might have led to variation in implantation locations among animals.

During pilot tests, we also observed several failure modes in chronically implanted animals: 1) motor deficits within 1 week post implantation caused by compressive spinal cord injury

Author Manuscript Author Manuscript Author Manuscript Author Manuscript

from dimpling during insertion. Animals with spinal cord injury symptoms such as paw dragging were excluded in this work and were avoided once surgeons had achieved proper technique. 2) channel impedance increases to >5 MΩ due to excessive force applied on the backend electronic connections during plug-in and plug-out; 3) impedance increases to approximately >2 MΩ (though could still record sortable spikes), likely caused by the regrowth of bone tissue that filled the epidural gap and encapsulated the reference electrode; 4) excessive motion noise coming from loosened backplate platforms.

Electrophysiological recording in behaving mice—Neural activity was recorded using an Intan amplifier headstage (RHD 64-Channel and 32-Channel Recording Headstages, Intan), an Intan recording controller (RHD USB Interface Board, Intan), and either an Intan RHX Data Acquisition Software (for data collected at Rice) or OpenEphys (for data collected at Salk). Before recording, we anesthetized the mice in 1.5%–2% isoflurane to safely connect the headstage to the PCB connector on the animals' back, through a custom-made PCB adaptor. After connection, mice were allowed to recover from anesthesia, and were then put either in home cage or on a treadmill without constraint. The home cage and treadmill were enclosed in a noise-attenuated, electrically shielded chamber. Prior to recording, we measured electrode impedances at 1 kHz. Then neural signals were recorded at a sampling rate of 30 kHz.

For behavior tests monitoring the joint angles, animals were put on a custom-built treadmill with transparent sidewalls. We placed a sideview camera to capture the animals' postures at either 200 fps (Salk) or 100 fps (Rice). To align the timelines of video frames and the electrophysiology recording, we connected the camera's TTL output (one pulse per frame) to the digital input of Intan acquisition board. For tests monitoring the hind paws, we used a treadmill with a transparent belt and a bottom-view camera (DigiGait, Mouse Specifics), with 50 fps and the same timeline alignment setup above. In both cases, the on/off status of the treadmill was closely monitored and adjusted to keep the animal running continuously but avoid exhausting the animal.

Spike sorting—Spike sorting was done using MountainSort. Raw signals were first filtered by a bandpass filter of 250–5000 Hz, followed by whitening (processor: ephys.whiten) and artifact removal (processor: ephys.mask_out_artifacts). Then in the spike sorter (processor: ms4alg.sort), spike detection threshold was set as 4 and detection sign was set as zero (to include both positive and negative spikes). The adjacency radius was set as 100 μm.

For studies involving characterizing neuronal waveforms or behavior-neuron correlations (i.e., Figure 2, 3, and 4), more stringent criteria is necessary to ensure single-unit isolation. Therefore, the output clusters from MountainSort were further examined manually to reject noise clusters and merge over-split clusters. The criteria of rejection and merging were agreed by three human judges. Specifically, we first rejected clusters with the following features: i) waveform amplitude less than 40 μV; or ii) waveforms with similar amplitude appeared on all electrodes; or iii) ISI violation percentage more than 7% at 2 ms (bursting units with higher ISI violation percentage were not rejected); or iv) severely distorted waveforms. We then merged clusters that share both: i) similar waveform shapes and

Author Manuscript Author Manuscript Author Manuscript Author Manuscript

amplitudes; and ii) similar waveform distribution across electrodes. After merging, we checked the ISI violations and cross-correlograms of merged putative units to further examine if there are over-merged and under-merged pairs.

For assessing the chronic performance of NET electrodes (Figure 5), due to the large number of clusters involved, we used an automatic algorithm to curate the output clusters from Mountainsort, instead of manual curation. This ensures consistent processing standard for different recording sessions. In the scripts we specified explicit rules and thresholds to reject noisy units and then merge over-split units. These rules are designed to imitate how a human inspector would make decisions; the parameters are determined empirically. The rules are as follows.

1. To exclude noise clusters, if any of the following criteria was satisfied, the putative unit was rejected:
    a. Signal-to-noise ratio less than 1.5
    b. Peak amplitude less than 50 μV
    c. Noise-overlap score (output from MountainSort) larger than 0.3
    d. Firing rate less than 0.05 Hz
    e. Amplitudes detected by far-away electrodes (≥ 140 μm from the primary electrode) exceeds 40% amplitude detected by the primary channel. (a modification from[77]
    f. ISI violation percentage larger than 7% at 2 ms.
2. Clusters that passed noise rejection were then examined by the merging criteria. Two clusters were merged if they met all the following conditions:
    a. The distance between 2 candidate clusters is less than 25 μm; (unit positions are estimated using the center-of-mass)
    b. Similarity of waveforms: The Pearson's R correlation coefficient between the template waveforms of 2 candidate clusters is larger than 0.7.
    c. The amplitude of one cluster is less than 1.5x of the other.
    d. If merged, the ISI violation percentage is less than 7% at 2 ms.

The merging procedure compares two clusters at each attempt and iteratively merges all qualifying candidate groups until they converge. Note that the rules are less stringent than human inspector's decision process, because falsely including over-split units is less fatal to chronic performance evaluation than to neuron-locomotion correlation. Consequently, the reported unit counts in the chronic assessment are slightly larger than typical human-curated sessions.

Visualization of cluster isolation in 3D space—To visualize how well the single units are isolated from each other, we applied dimension reduction to spike waveforms of 12 single units from 8 channels, through Uniform Manifold Approximation and Projection

Author Manuscript Author Manuscript Author Manuscript Author Manuscript

(UMAP) algorithm. Data were prepared by whitening waveform amplitudes using zero-phase component analysis (ZCA) to reduce feature redundancy and preserve its original phase with minimal compression. Decorrelation by ZCA required the following steps.

1. Standardizing through normalization and zero-centering:

$$Xnorm = a + [X - \min X \ \ \max X - \min X](b - a), [a,b] = [0, 1]$$

$$X_{centered} = X_{norm} - \frac{1}{N}\sum_{i=1}^{N} X_{norm}$$

2. Calculation of covariance:

$$\Sigma = \frac{1}{M}\sum_{i=1}^{n} (X^i_{centered})(X^i_{centered})^T$$

3. Singular Value Decomposition (SVD):

$$[U, S, V] = sv(\Sigma)$$

4. Zero-phase Component Analysis:

$$W_{ZCA} = U\Lambda^{-\frac{1}{2}}U^{\top}X_{centered}$$

$$\Lambda \ : \ diag(S) + \varepsilon$$

ε is simply a scaling regularization step.

After ZCA transformation, spikes were patched into vectors of ~3 ms waveforms (n = 8) from each channel in every identified cluster. The resulting concatenated amplitudes produced a 169591 x 800 (M x N) matrix. N was the total bin length of recorded spikes across 8 channels (100 bins/waveform, ~3.3ms) and M was the total patched spike vectors across all clusters. UMAP (v0.5.1[78]) was performed with cosine similarity as distance metric to embed the neural activity into 3 dimensions; additional parameters are listed in the table below.

UMAP parameters.

Metric	**‘Cosine’**
min_dist	0.1
n_neighbors	50
n_components	3

Author Manuscript Author Manuscript Author Manuscript Author Manuscript

Metrics of biophysical characteristics—We evaluated the neuronal properties of 561 putative single units by calculating first-level metrics, including trough-to-peak and rise time of autocorrelograms ACGs τ_{rise}, using MATLAB-based framework CellExplorer (Figures 2H–2J). The width of the spike waveform, otherwise known as "trough-to-peak" latency, is defined by the time interval (ms) between the trough and the following peak of the waveform. Average waveforms of each single unit were used for trough-to-peak calculation. Additionally, we computed the rise time of the ACG τ_{rise} to quantify burstiness of spiking for the average waveform of every detected single unit. CellExplorer calculates ACGs (from −50 ms to 50 ms) of each unit by using a triple exponential equation, where one exponential fits the rise time τ_{rise} of ACGs. We observed an average of 0.4-ms ACG τ_{rise}. We calculated SNR (Figure 2F) by calculating the ratio between the mean peak-to-peak amplitude of all waveforms in each cluster to 0.6745 × MAD.[43] Furthermore, we evaluated the isolation score (Figure 2G) after manual curation of detected units from each recorded session ($n = 2$) per animal. MountainSort was used to recalculate isolation score using the curated units of each animal, where isolation score was defined as[48]:

$$m_{isolation}(A) = 1 - \min_{clusters\ B} m_{overlap}(A, B)$$

Analysis of behavior-spike correlation—Videos of mice running on treadmill were processed by DeepLabCut.[54] Specifically, six joints – illac crest, hip, knee, ankle, metatarsophalangeal, and toe – were labeled in the sideview footages. Four paws and rear were labeled in the bottom-view footages. We considered frames of likelihood less than 0.8 (likelihood was given by DeepLabCut) as mislabeled frames and removed them from downstream analysis. Joint angles and angular velocities of hip, knee, and ankle were calculated for each frame from the coordinates returned by DeepLabCut. The timings of frames and unit firings were aligned through TTL pulses generated by camera trigger.

For moving vs. standing comparison (Figures 3A–3C), the time of moving-standing boundary was manually defined as the frame in which the treadmill came to stop. For each unit, its spiking waveforms were extracted from a 60-s window before and after the boundary, then averaged for comparison. We removed units that fired less than 20 times in this time window. The spectrogram in Figure 3C was calculated from the same time window with time resolution of 5 s.

For coherence analysis, the Chronux toolbox (http://chronux.org/) was used to compute the spectral coherence between the joint angle and spike timings. Spike-behavior coherence is a frequency-domain quantification of the similarity of dynamics between a spike train and a behavioral signal (marked by joint angle in this case). The Chronux toolbox calculates both the magnitude (C, [0 1]) and phase (phi) of coherence, and only the magnitude is of interest in this work. C represents the similarity of dynamics between two signals in the frequency domain. For example, C = 1 means the spike timings and oscillatory joint angle are strictly phase-locked, while C = 0 means there is no spectral correlation between them.

The angle-spike data were divided into multiple 5-s segments with the same underlying frequency of locomotion and high-pass filtered at 0.5 Hz. We used a frequency of interest

Author Manuscript Author Manuscript Author Manuscript Author Manuscript

at 2Hz for the recording session in Figure 3F, consistent with the observed oscillation frequency of knee angle. Then the coherence magnitude and phase of each unit was computed by Chronux, averaging all segments with a time-bandwidth product of 5 and tapers of 9. Because we used the average C computed from multiple 5-s trials, it is necessary to determine if the C value is statistically significant. The Chronux toolbox calculates the 95% confidence interval and the null value of C. The confidence interval means we are 95% confident that the true population value of C lies within this interval. The null value here refers to the C when the null hypothesis is true, i.e., there's no temporal correlation between the spikes and joint angle. Therefore, if the null value lies within the 95% confidence interval, the C of this unit is not significant. As a hypothetical example, C = 0.5 computed from 100 trials. And at p value = 0.05, Chronux will calculate the 95% confidence interval Cerr = [0.3 0.6], and the null value confC = 0.1. Then because the lower limit of Cerr = 0.3 > confC = 0.1. We can say the coherence = 0.5 is statistically significant. On the contrary, if confC = 0.4 > Cerr = 0.3, the coherence is not statistically significant.[79] Therefore, in this work, the coherence is determined as significant if the lower limit of the 95% confidence interval is larger than the null value computed by Chronux.

The tuning curves of each unit (firing rate vs. angle or angular velocity) were calculated through the following steps.

1. extract the firing counts within each frame (10 ms for 100 fps, 5 ms for 200 fps);
2. count how many and which frames fall into an angle/velocity bin (e.g., frame 3, 10, 15 fall into angle bin [10 20] degrees);
3. For this angle/velocity bin, firing rate (Hz) = sum of firing counts/(sum of frames x frame time). For example, if frame 3, 10, 15 has 10, 20, 30 firings, then firing rate = (10 + 20 + 30) firings/(3 frames x 5 ms).

Note sliding window method was used to plot the tuning curves to reflect the overall trend of tuning. For angle tuning, we used bin size of 20° and incremental step of 1°. For angular velocity tuning, the bin size is 500°/s and the incremental step is 50°/s.

Longitudinal tracking of single units—We followed previously reported Mutual-Nearest-Neighbor algorithm[60] to track units across days, specifically with the following steps.

1. For each unit, its template waveforms on all 32 electrodes were stitched together.
2. Across two consecutive days, we calculated the Euclidean distances between units' stitched waveforms. Specifically, we considered each waveform as a vector $A = (v_1, v_2, \ldots v_{3200})$, where v_i is the measured voltage at t_i – the amplifier sampling time. The Euclidean distance L between waveform A and $A' = (v_1', v_2', \ldots v_{3200}')$ was calculated as:

$$L^2 = (v_1 - v_1')^2 + (v_2 - v_2')^2 + \ldots + (v_{3200} - v_{3200}')^2$$

3. If unit A in day 1 is closest to unit A' in day 2, and A' is also closest to A, we consider A and A' are a pair of mutual nearest neighbors and should be linked.

Author Manuscript Author Manuscript Author Manuscript Author Manuscript

We applied the same procedure above to all consecutive days (i.e. day 1–2, day 2–3, … day 6–7). Figures 4 and S5 only show units that were linked across all days. For example, if a unit was linked through day 1–4 but failed to pair with a mutual nearest neighbor to day 5, we then did not consider this unit trackable.

We applied the same method from Ref[60] to quantify the relative distances of successfully linked unit pairs to other possible linked units (Figure 4D). Specifically, for a successfully linked pair (A, A'), the L^2 of all other possible linked pairs $(A, B'), (A, C'), \ldots (B, A'), (C, A')$, etc., were normalized to the L^2 of (A, A'). The normalized distances from all consecutive days contribute to the histogram in Figure 4D.

In Figure 4D, the distances of linked unit waveforms to all other possible linking unit waveforms ($n = 2880$), were normalized to the distances of linked unit waveforms ($n = 96$). The normalized distances are shown in the histogram. The red line marks unity, the distance of linked waveforms. Over 99% of all other possible linking waveforms lie to the right of the blue line (3.8 times unity).

In Figure 4G, each day's ISI is normalized to the total ISI count of that day, to reflect the distribution without influence from the daily fluctuations of absolute ISI count.

Estimation of unit locations—We followed the previously reported method to estimate unit locations from their waveform's spatial distribution.[59] Briefly, when a neuron fires, its action potential is detected by multiple electrodes with different peak-to-peak amplitudes, relating to the relative locations between the neuron and the electrodes. The amplitude decays as the action potential travels from the soma to electrodes. For each electrode, the amplitude is proportional to the reciprocal of distance traveled:

$$ptp_{electrode} = \frac{\alpha}{\sqrt{(x - x_{electrode})^2 + (z - z_{electrode})^2 + y^2}}$$

where α is the putative neuron's overall magnitude; (x, z) are the neuron's projective coordinates in the electrode plane; y is the orthogonal distance between the neuron and the electrode plane. Given the amplitude distribution on a set of electrodes C, the values of (x, y, z, α) were calculated by optimizing the following metric (optimization details can be found in[59]):

$$\sum_{i \in C} \left(ptp_i - \frac{\alpha}{\sqrt{(x - x_i)^2 + (z - z_i)^2 + y^2}} \right)^2$$

Execution of the above algorithm was performed using a customized script from SpikeInterface.[58]

Histology—Histological procedures were performed at the Salk Institute. To prepare the histology samples, mice were anesthetized in a CO_2 chamber and perfused transcardially with 50 mL of PBS (1X, 4°C) followed by 50 mL of 4% paraformaldehyde (4°C, Electron

Author Manuscript Author Manuscript Author Manuscript Author Manuscript

Microscopy Sciences, 100504–858). We then cleared the cement on the spinal plate with a dental drill, and removed the glass window with fine forceps. The polyimide shank outside the neural tissue was therefore exposed and was carefully cut with fine spring scissors. Then the spinal cord tissue with NET embedded inside (L1-L3) was extracted from the vertebrae and post-fixed in 4% PFA overnight at 4°C. After the post-fixation, the tissue was washed with PBS for 10 min followed by a 1–3 day incubation in 30% sucrose for cryoprotection (4°C). The lumbar spinal cord was then embedded in Tissue-Tek OCT (Sakura 4583) for cryosectioning onto glass slides (Fisherbrand Superfrost slides 12-550-15) in the longitudinal (rostral-caudal) plane – perpendicular to the insertion direction. The section thickness was 30 μm.

After cryostat sectioning, the spinal cord slices were first incubated in PBST (1X PBS with 0.3% Triton X- and 1% goat serum blocking buffer) with primary antibodies overnight at 4°C for astrocytes (mouse anti-GFAP, 1:250, Millipore MAB3402), microglia (rabbit anti-Iba1 1:200, Fujifilm 019–19741), and neurons (NeuroTrace 640/660 1:200, Invitrogen). The slices were then washed with PBS and incubated with secondary antibodies for 2 h at room temperature (donkey anti-mouse 488, 1:100, Invitgrogen A-21202; donkey anti-rabbit 594, 1:100, Invitrogen A-21207). After staining, the slices were mounted with a glass coverslip and Fluoromount-G (00-4958-02) before imaging.

Bright field and fluorescent images were acquire using an Olympus VS-120 virtual slide scanner microscope with a 20× objective (0.3 NA). For quantification of cell distribution (Figure 5F), the neurons, astrocytes, and microglia were automatically identified and counted from the fluorescent images using QuPath (https://qupath.github.io/). We used sliding bins to calculate cell density in Figure 5F, with bin size of 20 μm × 300 μm and sliding step of 1 μm.

QUANTIFICATION AND STATISTICAL ANALYSIS

All statistical analyses were performed in MATLAB (MathWorks, MA). Results and details of the statistical comparisons performed in the study including sample sizes were reported in the results section and figure legends. Two-sided Wilcoxon rank-sum test was used to compare within-unit and cross-unit waveform similarities in Figure 3D, and $p < 0.05$ was accepted as statistically different. The built-in significance calculator in Chronux (http://chronux.org/) was used to determine coherence significance in Figure 3F. The coherence is determined as significant if the lower limit of the 95% confidence interval is larger than the null value computed by Chronux. Two-sample two-tailed t test was used to compare cell densities of near-probe and far-away regions in Figure S6, and $p < 0.05$ was accepted as statistically different.

Supplementary Material

Refer to Web version on PubMed Central for supplementary material.

ACKNOWLEDGMENTS

C.X., L.L., and Y.W. would like to thank Dr. Timothy D. Harris for inspiring discussions, the Animal Resource Facility at Rice University for animal care and housing, and the Rice nanofabrication facility for support on the

Author Manuscript Author Manuscript Author Manuscript Author Manuscript

microfabrication. B.A.T. would like to thank Drs. David Kleinfeld, Jeff Moore, and Takaki Komiyama for advice and encouragement, Dr. David Kleinfeld for his suggestion to experiment with flexible recording probes, and Steve Barry and Anthony Artale for advice and machining custom parts. This work was funded by the National Institute of Neurological Disorders and Stroke, under R01NS102917 (to C.X.), U01NS115588 (to C.X.), U01NS131086 (to C.X.), and R01NS109361 (to L.L.); and by Rice University internal funds (to L.L. and C.X.). S.L.P. is the Benjamin H. Lewis chair in neuroscience at the Salk Institute. B.A.T. was supported by a grant from the Mary K. Chapman Foundation. The work was funded by R01NS123160 (to S.L.P.), R01NS108034 (to A.N.), and U19NS112959 (to S.L.P., A.N., and E.A.).

REFERENCES

1. Arber S. (2012). Motor circuits in action: specification, connectivity, and function. Neuron 74, 975–989. 10.1016/j.neuron.2012.05.011. [PubMed: 22726829]
2. Kiehn O. (2006). Locomotor circuits in the mammalian spinal cord. Annu. Rev. Neurosci 29, 279–306. 10.1146/annurev.neuro.29.051605.112910. [PubMed: 16776587]
3. Abraira VE, and Ginty DD (2013). The sensory neurons of touch. Neuron 79, 618–639. 10.1016/j.neuron.2013.07.051. [PubMed: 23972592]
4. Grillner S, and Jessell TM (2009). Measured motion: searching for simplicity in spinal locomotor networks. Curr. Opin. Neurobiol 19, 572–586. 10.1016/j.conb.2009.10.011. [PubMed: 19896834]
5. Jankowska E. (2008). Spinal interneuronal networks in the cat: elementary components. Brain Res. Rev 57, 46–55. 10.1016/j.brainresrev.2007.06.022. [PubMed: 17884173]
6. Fetz EE, Perlmutter SI, and Prut Y (2000). Functions of mammalian spinal interneurons during movement. Curr. Opin. Neurobiol 10, 699–707. 10.1016/s0959-4388(00)00160-4. [PubMed: 11240278]
7. Gatto G, Smith KM, Ross SE, and Goulding M (2019). Neuronal diversity in the somatosensory system: bridging the gap between cell type and function. Curr. Opin. Neurobiol 56, 167–174. 10.1016/j.conb.2019.03.002. [PubMed: 30953870]
8. Russ DE, Cross RBP, Li L, Koch SC, Matson KJE, Yadav A, Alkaslasi MR, Lee DI, Le Pichon CE, Menon V, and Levine AJ (2021). A harmonized atlas of mouse spinal cord cell types and their spatial organization. Nat. Commun 12, 5722. 10.1038/s41467-021-25125-1. [PubMed: 34588430]
9. Osseward PJ, and Pfaff SL (2019). Cell type and circuit modules in the spinal cord. Curr. Opin. Neurobiol 56,175–184. 10.1016/j.conb.2019.03.003. [PubMed: 30954861]
10. Kiehn O. (2016). Decoding the organization of spinal circuits that control locomotion. Nat. Rev. Neurosci 17, 224–238. 10.1038/nrn.2016.9. [PubMed: 26935168]
11. Miri A, Azim E, and Jessell TM (2013). Edging toward entelechy in motor control. Neuron 80, 827–834. 10.1016/j.neuron.2013.10.049. [PubMed: 24183031]
12. Koch SC, Acton D, and Goulding M (2018). Spinal Circuits for Touch, Pain, and Itch. Annu. Rev. Physiol 80, 189–217. 10.1146/annurev-physiol-022516-034303. [PubMed: 28961064]
13. Luo L, Callaway EM, and Svoboda K (2018). Genetic Dissection of Neural Circuits: A Decade of Progress. Neuron 98, 256–281. 10.1016/j.neuron.2018.03.040. [PubMed: 29673479]
14. Nelson NA, Wang X, Cook D, Carey EM, and Nimmerjahn A (2019). Imaging spinal cord activity in behaving animals. Exp. Neurol 320, 112974. 10.1016/j.expneurol.2019.112974. [PubMed: 31175843]
15. Shekhtmeyster P, Carey EM, Duarte D, Ngo A, Gao G, Nelson NA, Clark CL, and Nimmerjahn A (2023). Multiplex translaminar imaging in the spinal cord of behaving mice. Nat. Commun 14, 1427. 10.1038/s41467-023-36959-2. [PubMed: 36944637]
16. Schiller J, Helmchen F, and Sakmann B (1995). Spatial profile of dendritic calcium transients evoked by action potentials in rat neocortical pyramidal neurones. J. Physiol 487, 583–600. 10.1113/jphysiol.1995.sp020902. [PubMed: 8544123]
17. Jiang L, Woodington B, Carnicer-Lombarte A, Malliaras G, and Barone DG (2022). Spinal cord bioelectronic interfaces: opportunities in neural recording and clinical challenges. J. Neural. Eng 19. 10.1088/1741-2552/ac605f.
18. Karimi A, Shojaei A, and Tehrani P (2017). Mechanical properties of the human spinal cord under the compressive loading. J. Chem. Neuroanat 86, 15–18. 10.1016/j.jchemneu.2017.07.004. [PubMed: 28720407]

Author Manuscript Author Manuscript Author Manuscript Author Manuscript

19. Rivnay J, Wang H, Fenno L, Deisseroth K, and Malliaras GG (2017). Next-generation probes, particles, and proteins for neural interfacing. Sci. Adv 3, e1601649. 10.1126/sciadv.1601649. [PubMed: 28630894]
20. Barrese JC, Aceros J, and Donoghue JP (2016). Scanning electron microscopy of chronically implanted intracortical microelectrode arrays in non-human primates. J. Neural. Eng 13, 026003. 10.1088/1741-2560/13/2/026003. [PubMed: 26824680]
21. Jiang Z, Carlin KP, and Brownstone RM (1999). An in vitro functionally mature mouse spinal cord preparation for the study of spinal motor networks. Brain Res. 816, 493–499. 10.1016/s0006-8993(98)01199-8. [PubMed: 9878874]
22. Schmidt BJ (1994). Afterhyperpolarization modulation in lumbar motoneurons during locomotor-like rhythmic activity in the neonatal rat spinal cord in vitro. Exp. Brain Res 99, 214–222. 10.1007/bf00239588. [PubMed: 7925804]
23. Hachisuka J, Baumbauer KM, Omori Y, Snyder LM, Koerber HR, and Ross SE (2016). Semi-intact ex vivo approach to investigate spinal somatosensory circuits. Elife 5, e22866. 10.7554/eLife.22866. [PubMed: 27991851]
24. Urch CE, and Dickenson AH (2003). In vivo single unit extracellular recordings from spinal cord neurones of rats. Brain Res. Protoc 12, 26–34. 10.1016/S1385-299X(03)00068-0.
25. Jordan LM, Pratt CA, and Menzies JE (1979). Locomotion evoked by brain stem stimulation: occurrence without phasic segmental afferent input. Brain Res. 177, 204–207. 10.1016/0006-8993(79)90933-8. [PubMed: 497822]
26. Kashkoush AI, Gaunt RA, Fisher LE, Bruns TM, and Weber DJ (2019). Recording single- and multi-unit neuronal action potentials from the surface of the dorsal root ganglion. Sci. Rep 9, 2786. 10.1038/s41598-019-38924-w. [PubMed: 30808921]
27. Lindén H, Petersen PC, Vestergaard M, and Berg RW (2022). Movement is governed by rotational neural dynamics in spinal motor networks. Nature 610, 526–531. 10.1038/s41586-022-05293-w. [PubMed: 36224394]
28. Perlmutter SI, Maier MA, and Fetz EE (1998). Activity of Spinal Interneurons and Their Effects on Forearm Muscles During Voluntary Wrist Movements in the Monkey. J. Neurophysiol 80, 2475–2494. 10.1152/jn.1998.80.5.2475. [PubMed: 9819257]
29. Prut Y, and Fetz EE (1999). Primate spinal interneurons show pre-movement instructed delay activity. Nature 401, 590–594. 10.1038/44145. [PubMed: 10524626]
30. Hadzipasic M, Ni W, Nagy M, Steenrod N, McGinley MJ, Kaushal A, Thomas E, McCormick DA, and Horwich AL (2016). Reduced high-frequency motor neuron firing, EMG fractionation, and gait variability in awake walking ALS mice. Proc. Natl. Acad. Sci. USA 113, E7600–E7609. 10.1073/pnas.1616832113. [PubMed: 27821773]
31. Maier MA, Perlmutter SI, and Fetz EE (1998). Response patterns and force relations of monkey spinal interneurons during active wrist movement. J. Neurophysiol 80, 2495–2513. 10.1152/jn.1998.80.5.2495. [PubMed: 9819258]
32. Seki K, Perlmutter SI, and Fetz EE (2003). Sensory input to primate spinal cord is presynaptically inhibited during voluntary movement. Nat. Neurosci 6, 1309–1316. 10.1038/nn1154. [PubMed: 14625555]
33. Glenn LL, and Dement WC (1981). Membrane potential, synaptic activity, and excitability of hindlimb motoneurons during wakefulness and sleep. J. Neurophysiol 46, 839–854. 10.1152/jn.1981.46.4.839. [PubMed: 7288467]
34. Lu C, Park S, Richner TJ, Derry A, Brown I, Hou C, Rao S, Kang J, Mortiz CT, Fink Y, and Anikeeva P (2017). Flexible and stretchable nanowire-coated fibers for optoelectronic probing of spinal cord circuits. Sci. Adv 3, e1600955. 10.1126/sciadv.1600955. [PubMed: 28435858]
35. Liu X, Xu Z, Fu X, Liu Y, Jia H, Yang Z, Zhang J, Wei S, and Duan X (2022). Stable, long-term single-neuronal recording from the rat spinal cord with flexible carbon nanotube fiber electrodes. J. Neural. Eng 19. 10.1088/1741-2552/ac9258.
36. and, J.R.W., and Tennissen AM (2001). Activity-Dependent Spinal Cord Plasticity in Health and Disease. Annu. Rev. Neurosci 24, 807–843. 10.1146/annurev.neuro.24.1.807. [PubMed: 11520919]

Author Manuscript Author Manuscript Author Manuscript Author Manuscript

37. Kleinfeld D, Luan L, Mitra PP, Robinson JT, Sarpeshkar R, Shepard K, Xie C, and Harris TD (2019). Can One Concurrently Record Electrical Spikes from Every Neuron in a Mammalian Brain? Neuron 103, 1005–1015. 10.1016/j.neuron.2019.08.011. [PubMed: 31495645]
38. He F, Sun Y, Jin Y, Yin R, Zhu H, Rathore H, Xie C, and Luan L (2022). Longitudinal neural and vascular recovery following ultraflexible neural electrode implantation in aged mice. Biomaterials 291, 121905. 10.1016/j.biomaterials.2022.121905. [PubMed: 36403326]
39. Luan L, Wei X, Zhao Z, Siegel JJ, Potnis O, Tuppen CA, Lin S, Kazmi S, Fowler RA, Holloway S, et al. (2017). Ultraflexible nanoelectronic probes form reliable, glial scar–free neural integration. Sci. Adv 3, e1601966. 10.1126/sciadv.1601966. [PubMed: 28246640]
40. Sekiguchi KJ, Shekhtmeyster P, Merten K, Arena A, Cook D, Hoffman E, Ngo A, and Nimmerjahn A (2016). Imaging large-scale cellular activity in spinal cord of freely behaving mice. Nat. Commun 7, 11450. 10.1038/ncomms11450. [PubMed: 27121084]
41. Farrar MJ, Bernstein IM, Schlafer DH, Cleland TA, Fetcho JR, and Schaffer CB (2012). Chronic in vivo imaging in the mouse spinal cord using an implanted chamber. Nat. Methods 9, 297–302. [PubMed: 22266542]
42. Yang L, Lee K, Villagracia J, and Masmanidis SC (2020). Open source silicon microprobes for high throughput neural recording. J. Neural. Eng 17, 016036. 10.1088/1741-2552/ab581a. [PubMed: 31731284]
43. Jun JJ, Steinmetz NA, Siegle JH, Denman DJ, Bauza M, Barbarits B, Lee AK, Anastassiou CA, Andrei A, Aydin Ç, et al. (2017). Fully integrated silicon probes for high-density recording of neural activity. Nature 551, 232–236. 10.1038/nature24636. [PubMed: 29120427]
44. Rizk M, Bossetti CA, Jochum TA, Callender SH, Nicolelis MAL, Turner DA, and Wolf PD (2009). A fully implantable 96-channel neural data acquisition system. J. Neural. Eng 6, 026002. 10.1088/1741-2560/6/2/026002. [PubMed: 19255459]
45. Rennaker RL, Ruyle AM, Street SE, and Sloan AM (2005). An economical multi-channel cortical electrode array for extended periods of recording during behavior. J. Neurosci. Methods 142, 97–105. 10.1016/j.jneumeth.2004.07.018. [PubMed: 15652622]
46. Williams JC, Rennaker RL, and Kipke DR (1999). Long-term neural recording characteristics of wire microelectrode arrays implanted in cerebral cortex. Brain Res. Protoc 4, 303–313. 10.1016/S1385-299X(99)00034-3.
47. Fiáth R, Márton AL, Mátyás F, Pinke D, Márton G, Tóth K, and Ulbert I (2019). Slow insertion of silicon probes improves the quality of acute neuronal recordings. Sci. Rep 9, 111. 10.1038/s41598-018-36816-z. [PubMed: 30643182]
48. Chung JE, Magland JF, Barnett AH, Tolosa VM, Tooker AC, Lee KY, Shah KG, Felix SH, Frank LM, and Greengard LF (2017). A Fully Automated Approach to Spike Sorting. Neuron 95, 1381–1394.e6. 10.1016/j.neuron.2017.08.030. [PubMed: 28910621]
49. Rossant C, Kadir SN, Goodman DFM, Schulman J, Hunter MLD, Saleem AB, Grosmark A, Belluscio M, Denfield GH, Ecker AS, et al. (2016). Spike sorting for large, dense electrode arrays. Nat. Neurosci 19, 634–641. 10.1038/nn.4268. [PubMed: 26974951]
50. Hill DN, Mehta SB, and Kleinfeld D (2011). Quality Metrics to Accompany Spike Sorting of Extracellular Signals. J. Neurosci 31, 8699–8705. 10.1523/jneurosci.0971-11.2011. [PubMed: 21677152]
51. Petersen PC, Siegle JH, Steinmetz NA, Mahallati S, and Buzsáki G (2021). CellExplorer: A framework for visualizing and characterizing single neurons. Neuron 109, 3594–3608.e2. 10.1016/j.neuron.2021.09.002. [PubMed: 34592168]
52. Nicolai EN, Michelson NJ, Settell ML, Hara SA, Trevathan JK, Asp AJ, Stocking KC, Lujan JL, Kozai TDY, and Ludwig KA (2018). Design Choices for Next-Generation Neurotechnology Can Impact Motion Artifact in Electrophysiological and Fast-Scan Cyclic Voltammetry Measurements. Micromachines 9, 494. 10.3390/mi9100494. [PubMed: 30424427]
53. Orlovsky G, Deliagina TG, and Grillner S (1999). Neuronal Control of Locomotion: From Mollusc to Man (Oxford University Press). 10.1093/acprof:oso/9780198524052.001.0001.
54. Mathis A, Mamidanna P, Cury KM, Abe T, Murthy VN, Mathis MW, and Bethge M (2018). DeepLabCut: markerless pose estimation of user-defined body parts with deep learning. Nat. Neurosci 21, 12811289. 10.1038/s41593-018-0209-y.

Author Manuscript Author Manuscript Author Manuscript Author Manuscript

55. Bokil H, Andrews P, Kulkarni JE, Mehta S, and Mitra PP (2010). Chronux: a platform for analyzing neural signals. J. Neurosci. Methods 192, 146–151. 10.1016/j.jneumeth.2010.06.020. [PubMed: 20637804]
56. Moore JD, Deschênes M, Furuta T, Huber D, Smear MC, Demers M, and Kleinfeld D (2013). Hierarchy of orofacial rhythms revealed through whisking and breathing. Nature 497, 205–210. 10.1038/nature12076. [PubMed: 23624373]
57. Takatoh J, Prevosto V, Thompson PM, Lu J, Chung L, Harrahill A, Li S, Zhao S, He Z, Golomb D, et al. (2022). The whisking oscillator circuit. Nature 609, 560–568. 10.1038/s41586-022-05144-8. [PubMed: 36045290]
58. Buccino AP, Hurwitz CL, Garcia S, Magland J, Siegle JH, Hurwitz R, and Hennig MH (2020). SpikeInterface, a unified framework for spike sorting. Elife 9, e61834. 10.7554/eLife.61834. [PubMed: 33170122]
59. Boussard J, Varol E, Lee HD, Dethe N, and Paninski L (2021). Three-dimensional spike localization and improved motion correction for Neuropixels recordings. bioRxiv. 10.1101/2021.11.05.467503.
60. Chung JE, Joo HR, Fan JL, Liu DF, Barnett AH, Chen S, Gea-ghan-Breiner C, Karlsson MP, Karlsson M, Lee KY, et al. (2019). High-Density, Long-Lasting, and Multi-region Electrophysiological Recordings Using Polymer Electrode Arrays. Neuron 101, 21–31.e5. 10.1016/j.neuron.2018.11.002. [PubMed: 30502044]
61. Letner JG, Patel PR, Hsieh J-C, Smith Flores IM, della Valle E, Walker LA, Weiland JD, Chestek CA, and Cai D (2023). Postexplant profiling of subcellular-scale carbon fiber intracortical electrodes and surrounding neurons enables modeling of recorded electrophysiology. J. Neural. Eng 20, 026019. 10.1088/1741-2552/acbf78.
62. Steinmetz NA, Aydin C, Lebedeva A, Okun M, Pachitariu M, Bauza M, Beau M, Bhagat J, Böhm C, Broux M, et al. (2021). Neuropixels 2.0: A miniaturized high-density probe for stable, longterm brain recordings. Science 372, eabf4588. 10.1126/science.abf4588. [PubMed: 33859006]
63. Zhao Z, Luan L, Wei X, Zhu H, Li X, Lin S, Siegel JJ, Chitwood RA, and Xie C (2017). Nanoelectronic Coating Enabled Versatile Multifunctional Neural Probes. Nano Lett. 17, 4588–4595. 10.1021/acs.nanolett.7b00956. [PubMed: 28682082]
64. He F, Sullender CT, Zhu H, Williamson MR, Li X, Zhao Z, Jones TA, Xie C, Dunn AK, and Luan L (2020). Multimodal mapping of neural activity and cerebral blood flow reveals long-lasting neurovascular dis-sociations after small-scale strokes. Sci. Adv 6, eaba1933. 10.1126/sciadv.aba1933. [PubMed: 32494746]
65. Zhao Z, Zhu H, Li X, Sun L, He F, Chung JE, Liu DF, Frank L, Luan L, and Xie C (2023). Ultraflexible electrode arrays for months-long high-density electrophysiological mapping of thousands of neurons in rodents. Nat. Biomed. Eng 7, 520–532. 10.1038/s41551-022-00941-y. [PubMed: 36192597]
66. Lee AK, Manns ID, Sakmann B, and Brecht M (2006). Whole-cell recordings in freely moving rats. Neuron 51, 399–407. 10.1016/j.neuron.2006.07.004. [PubMed: 16908406]
67. Ravassard P, Kees A, Willers B, Ho D, Aharoni DA, Cushman J, Aghajan ZM, and Mehta MR (2013). Multisensory control of hippocam-pal spatiotemporal selectivity. Science (New York, N.Y.) 340, 1342–1346. 10.1126/science.1232655. [PubMed: 23641063]
68. Alaynick WA, Jessell TM, and Pfaff SL (2011). SnapShot: spinal cord development. Cell 146, 178–178.e1. 10.1016/j.cell.2011.06.038. [PubMed: 21729788]
69. Bikoff JB, Gabitto MI, Rivard AF, Drobac E, Machado TA, Miri A, Brenner-Morton S, Famojure E, Diaz C, Alvarez FJ, et al. (2016). Spinal Inhibitory Interneuron Diversity Delineates Variant Motor Microcircuits. Cell 165, 207–219. 10.1016/j.cell.2016.01.027. [PubMed: 26949184]
70. Brownstone RM, and Bui TV (2010). Spinal interneurons providing input to the final common path during locomotion. Prog. Brain Res 187, 81–95. 10.1016/b978-0-444-53613-6.00006-x. [PubMed: 21111202]
71. Dhawale AK, Poddar R, Wolff SB, Normand VA, Kopelowitz E, and Ölveczky BP (2017). Automated long-term recording and analysis of neural activity in behaving animals. Elife 6, e27702. 10.7554/eLife.27702. [PubMed: 28885141]

Author Manuscript Author Manuscript Author Manuscript Author Manuscript

72. Eleryan A, Vaidya M, Southerland J, Badreldin IS, Balasubramanian K, Fagg AH, Hatsopoulos N, and Oweiss K (2014). Tracking single units in chronic, large scale, neural recordings for brain machine interface applications. Front. Neuroeng 7, 23. 10.3389/fneng.2014.00023. [PubMed: 25071546]

73. Wei X, Luan L, Zhao Z, Li X, Zhu H, Potnis O, and Xie C (2018). Nanofabricated Ultraflexible Electrode Arrays for High-Density Intracortical Recording. Adv. Sci 5, 1700625. 10.1002/advs.201700625.

74. Fournely M, Petit Y, Wagnac E, Evin M, and Arnoux PJ (2020). Effect of experimental, morphological and mechanical factors on the murine spinal cord subjected to transverse contusion: A finite element study. PLoS One 15, e0232975. 10.1371/journal.pone.0232975. [PubMed: 32392241]

75. Rongkang Y, Brian CN, Fei H, Pavlo Z, Haad R, Yifu J, Nicole S, Chong X, and Lan L (2022). Chronic co-implantation of ultraflexible neural electrodes and a cranial window. Neurophotonics 9, 1–13. 10.1117/1.NPh.9.3.032204.

76. Farrar MJ, Bernstein IM, Schlafer DH, Cleland TA, Fetcho JR, and Schaffer CB (2012). Chronic in vivo imaging in the mouse spinal cord using an implanted chamber. Nat. Methods 9, 297–302. 10.1038/nmeth.1856. [PubMed: 22266542]

77. Siegle JH, Jia X, Durand S, Gale S, Bennett C, Graddis N, Heller G, Ramirez TK, Choi H, Luviano JA, et al. (2021). Survey of spiking in the mouse visual system reveals functional hierarchy. Nature 592, 86–92. 10.1038/s41586-020-03171-x. [PubMed: 33473216]

78. Mclnnes L, Healy J, Großberger L, and Großberger L (2018). UMAP: Uniform Manifold Approximation and Projection. J. Open Source Softw. 3, 861. 10.21105/joss.00861.

79. Bokil K.P.P.a.H. (2008). Neural Signal Processing Tutorial 1. In Neural Signal Processing: Quantitative Analysis of Neural Activity, P M, ed., pp. 73–75.

Author Manuscript Author Manuscript Author Manuscript Author Manuscript

Highlights

- Ultraflexible electrodes in the ventral laminae adapt to spinal cord motion
- High SNR spikes from unrestrained, behaving mice resolve well-isolated single units
- Functional tuning to hindlimb locomotion reveals diverse patterns of neural activity
- Stable electrode-tissue interface enables longitudinal tracking of single units

Author Manuscript Author Manuscript Author Manuscript Author Manuscript

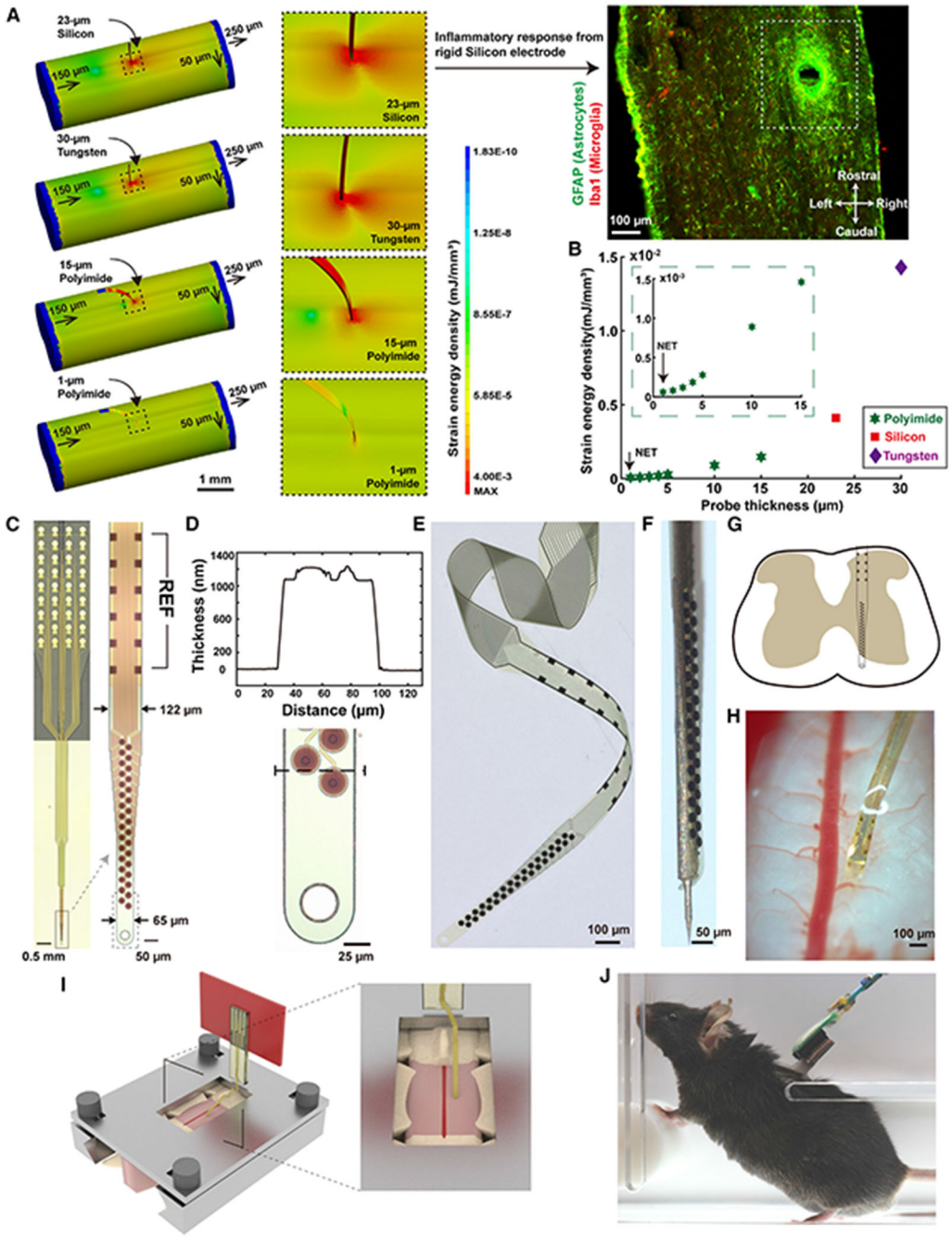

Figure 1. Customized 32-channel ultraflexible *intraspinal* NET for the highly mobile spinal cord

(A) Left: distribution of strain energy density in a segment of spinal tissue with four types of electrodes: Si probe of 23 × 85 μm^2 cross-sectional area, 30-μm-diameter tungsten microwire, 15-μm-thick PI probe, and 1-μm-thick NET. The direction and magnitude of rostral-caudal and medial-lateral displacements are marked by black arrows. Right: immunofluorescence image of spinal cord tissue at 28 days post 23-μm-thick Si probe implantation (overlay of GFAP and Iba1). The dashed rectangle refers to the implantation site.

Author Manuscript Author Manuscript Author Manuscript Author Manuscript

(B) The relationship between strain energy density at the probe-tissue interface and various probe materials and thicknesses. Inset: zoom-in plot of PI probes of 1–15 μm thickness. The arrow denotes NET with a thickness of 1 μm.
(C) Left: image of a 32-channel NET on a fused silica substrate. Right: zoom-in image showing the layout of recording contacts and reference contacts.
(D) Top: profilometry measurement of NET's thickness at the location indicated by the dashed line in the bottom. Bottom: zoom-in image of the dashed rectangle in (C) right.
(E) Image of NET's ultraflexible thread immersed in water after being released from the substrate.
(F) Image of a NET threaded onto a micromachined tungsten needle for delivery into the spinal cord.
(G) Transverse-plane schematic of the approximate implantation location in the spinal cord.
(H) Image of a NET implanted in the spinal cord.
(I) Overview schematic of the implanted components, including two sidebars clamped onto the vertebrae and a top plate for mounting the backstage. The zoom-in sketch at the implantation site highlights a flexible section with redundant length outside the tissue to accommodate micromotions of the spinal cord when the animal is moving.
(J) Photo of a rearing mouse carrying a recording backstage with a NET implanted in its lumbar cord.

Author Manuscript Author Manuscript Author Manuscript Author Manuscript

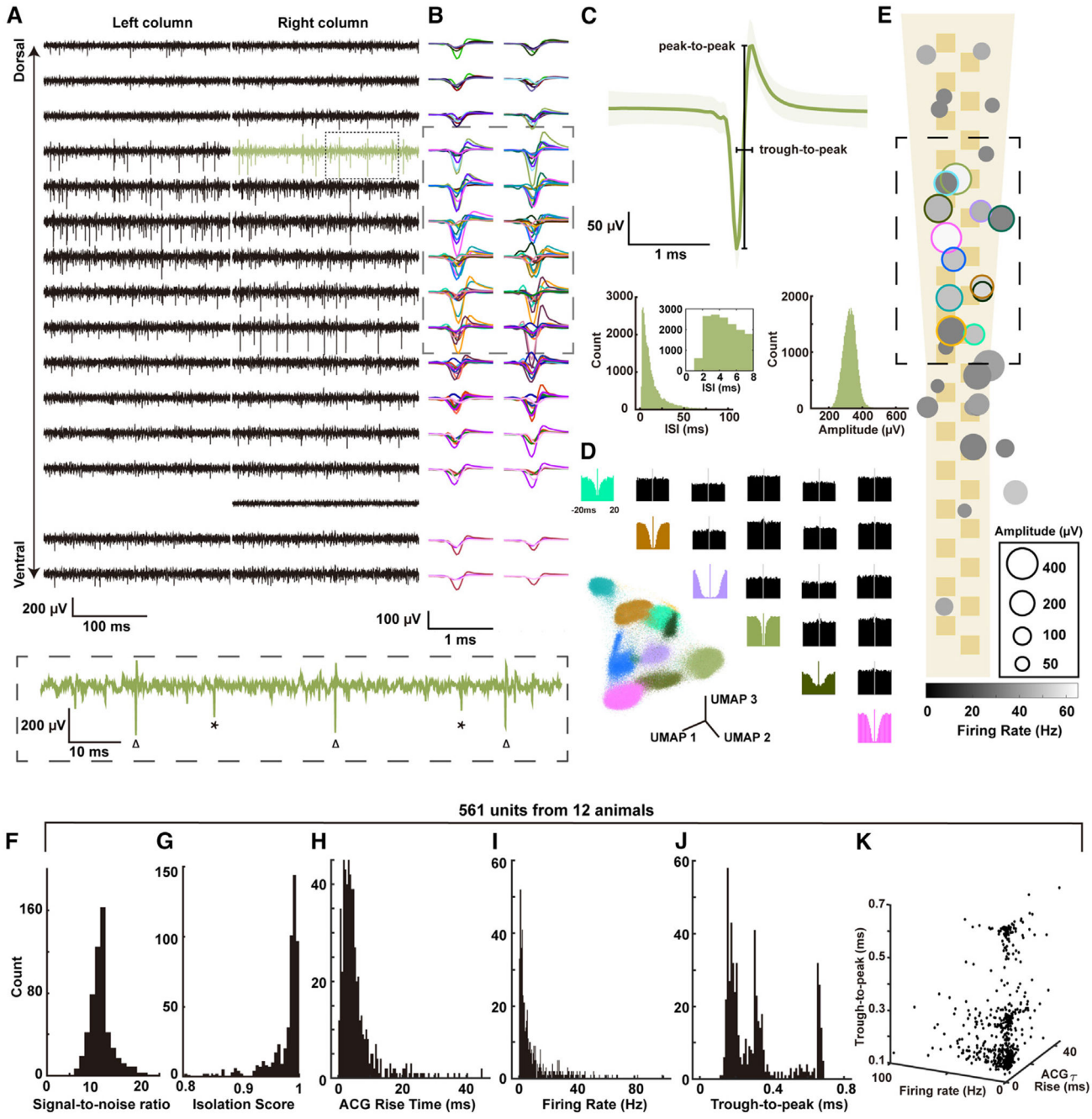

Figure 2. Diverse waveform characteristics in many well-isolated single units

(A) Representative recordings (bandpass filtered at 200–7,000 Hz) from a 32-channel NET implanted in the lumbar (L1-L2) spinal cord of an awake, freely moving mouse. The zoom-in trace at the bottom (green) shows the recording of a representative channel (green, top), where * and Δ mark the spikes of two different units.

(B) Average waveforms across all channels for each single unit. Each color represents one unit. The dashed box marks the segment used in (D).

Author Manuscript Author Manuscript Author Manuscript Author Manuscript

(C) Waveform (top), inter-spike interval (ISI) distribution (bottom left), and amplitude distribution (bottom right) of a representative single unit.
(D) 3D UMAP showing the clustering of 12 single units recorded by 8 contacts, and the ACGs and CCGs of 6 representative units.
(E) Amplitudes, firing rate, and approximate location (estimated by triangulation) of all single units. The dashed box marks the identical segment as in (B). (A–E) Are from the same recording section, and units are color matched in (B–E).
(F–J) Distribution of signal-to-noise ratio (F), isolation score (G), ACG rise time (H), firing rate (I), trough-to-peak time (J), and joint distribution of features (K) of all single units recorded from $n = 12$ animals, two recording sessions per animal.

Author Manuscript Author Manuscript Author Manuscript Author Manuscript

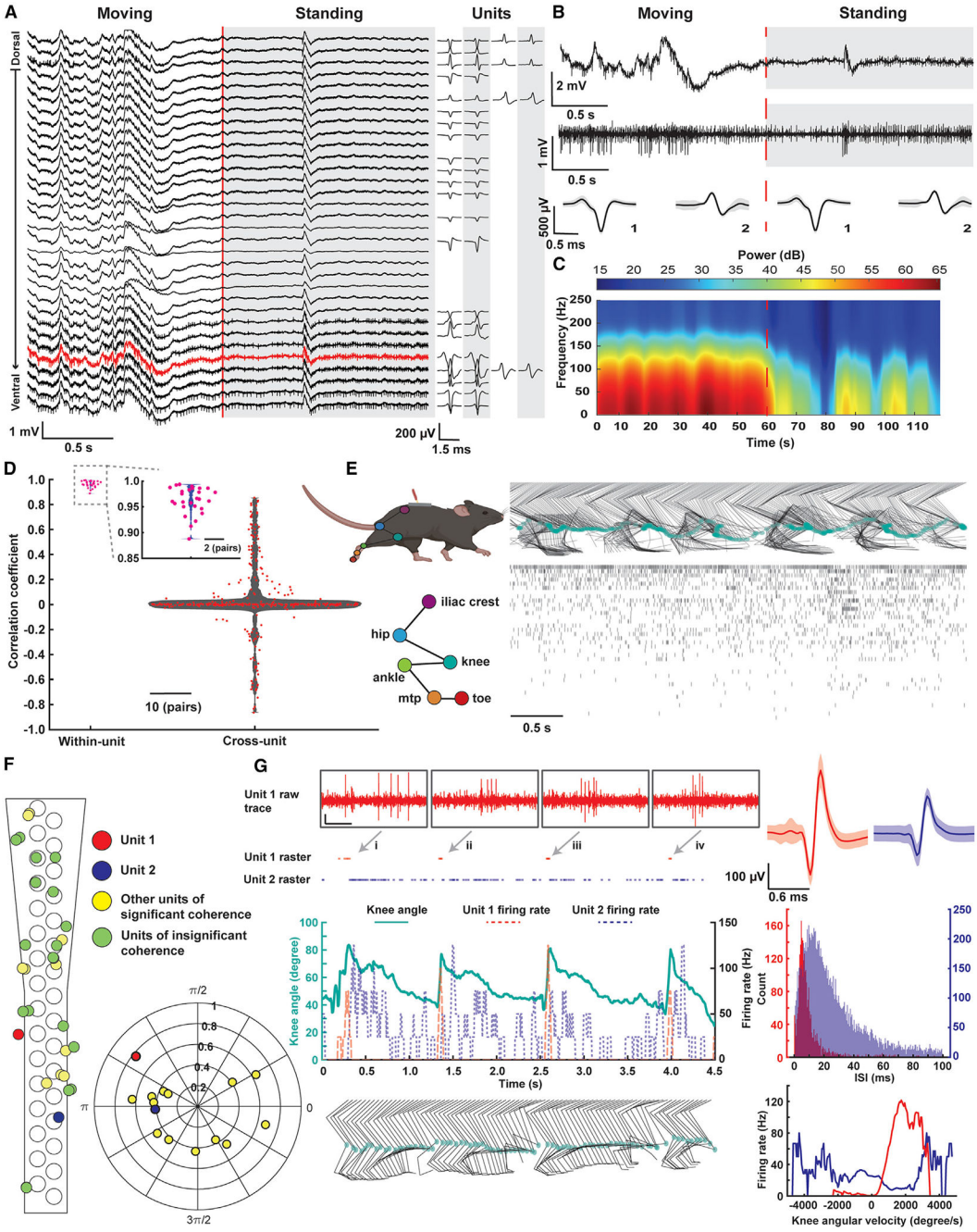

Figure 3. Accommodating spinal cord motion allows for determination of unit-locomotion relationship

(A) Representative broadband recordings (left) and averaged waveforms of sorted units (right) from all channels at the transition from moving (unshaded) and standing (shaded) states. Channels are arranged from dorsal to ventral. Unit waveforms are aligned with their primary channels (moving, unshaded; standing, shaded).

(B) Broadband voltage signal (top), high-pass (>300 Hz) filtered voltage signal (middle), and the averaged waveform and standard deviations (shade) of two units detected (bottom) from one recording channel marked as red in (A).

Author Manuscript Author Manuscript Author Manuscript Author Manuscript

(C) Spectrogram of local field potentials of the same channel in (B). The switch between moving and standing occurred at t = 60 s and is marked as a red dashed line.
(D) Distribution of correlation coefficients between unit waveforms from moving and standing states. Within-unit compares the same units between moving and standing states. Cross-unit compares different units between moving and standing states.
(E) A representative animal showing the labeling and extraction of multiple joints from a side view video (left, schematic adapted from “Mouse (running)” by BioRender.com), strike dynamics (right top), and firing timestamps from all units in alignment with the strike dynamics (right bottom).
(F) Left: estimated locations of single units of both significant and insignificant coherence to measured knee angle. Right: polar plot of the magnitude (0–1 radial coordinate) and phase (angular coordinate) of the coherence between single unit spiking activity and measured knee angle at a frequency of 2 Hz. Only units with significant coherence ($p < 0.05$) are shown and correspond to the estimated locations in the left panel. Units 1 and 2 are the same units shown in (G).
(G) Two representative units showed distinctive firing patterns in correlation with the dynamics of the knee angle. All features of unit 1 and unit 2 are color coded as red and blue, respectively. Left (top to bottom): zoom-in raw trace of the primary electrode that recorded unit 1, scale 50 ms/100 μV; spike raster of unit 1 and unit 2; knee angle dynamics (cyan) and firing rates of unit 1 and unit 2; strike dynamics with the knee color coded as cyan dots. The spike raster, knee angle, firing rates, and strike dynamics are all temporally aligned. Right (top to bottom): average waveforms (shade presents SD), ISI histograms, and firing rate-angular velocity relationships of unit 1 and unit 2.

Author Manuscript Author Manuscript Author Manuscript Author Manuscript

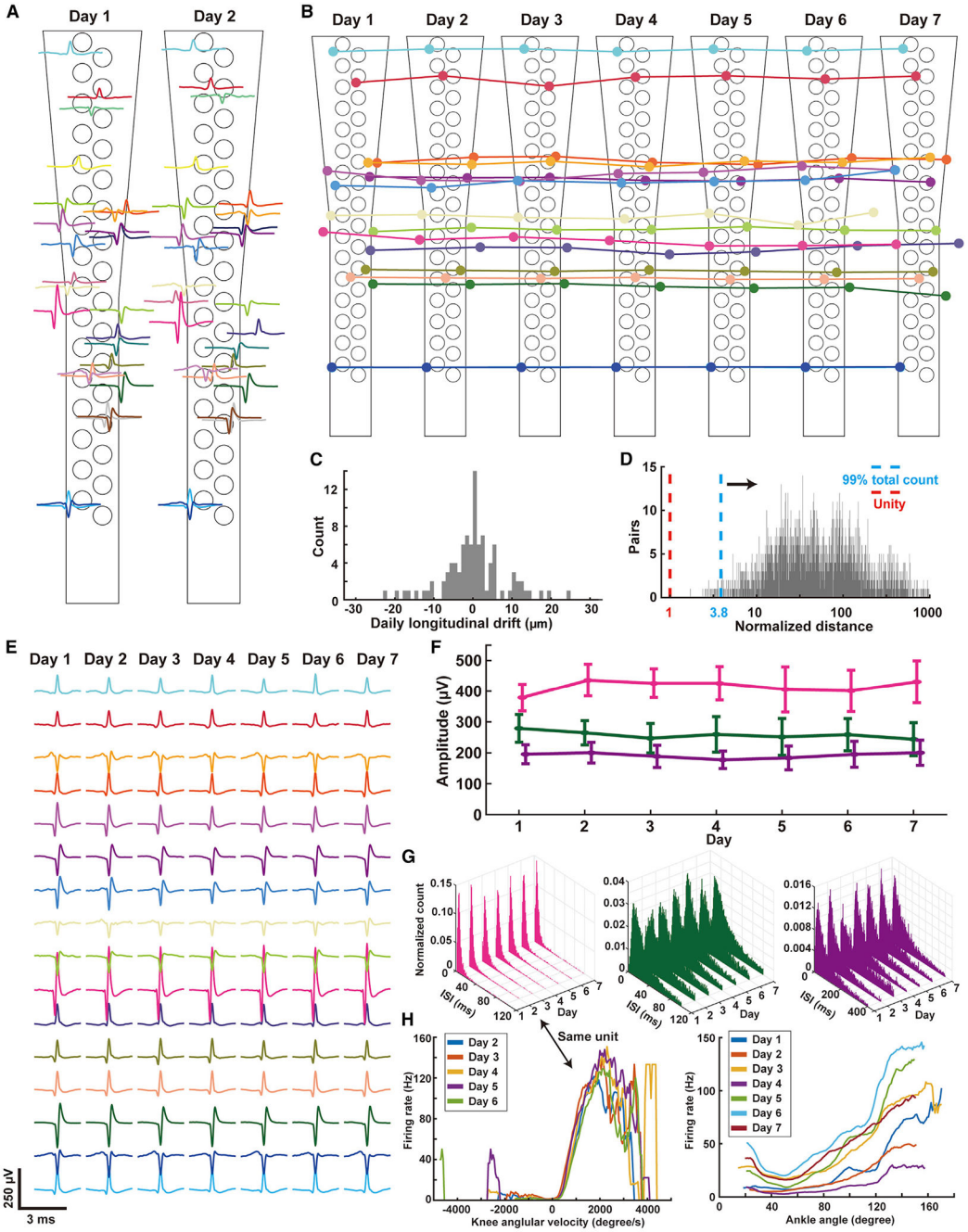

Figure 4. Stable unit tracking and reproducible behavioral tuning across 7 days in task-performing mice

(A) The tracking of units from day 1 to 2 in a running mouse. The waveforms of a total of 25 units are placed on the estimated coordinates based on triangulation, with matching colors indicating the same units.

(B) Estimated locations of the 16 trackable units (solid dots) relative to the NET across all 7 days, with lines connecting the locations of the same units to depict day-to-day position drift.

Author Manuscript Author Manuscript Author Manuscript Author Manuscript

(C) Histogram of the drift distances (the spatial drift for each day for each unit along the longitudinal direction of the thread) between consecutive days of all trackable units.
(D) Histogram of the Euclidean distance in the feature space between any two unmatched units detected on 7 consecutive days. Blue dashed line marks the normalized distance of 3.8 for which 99% of the unmatched pairs surpass. Red dashed line marks unity.
(E) Average waveforms of the 16 trackable units from days 1 to 7.
(F) Average amplitudes and standard deviations of three exemplary units across 7 days (n = 1 animal).
(G) Seven-day ISI histograms of the three units in (F). Units shown in (A), (B), and (E)–(G) are color-matched. (H) Example of two units exhibiting consistent tuning curves to the knee angular velocity (left) and to the ankle angle (right) across multiple days.

Author Manuscript Author Manuscript Author Manuscript Author Manuscript

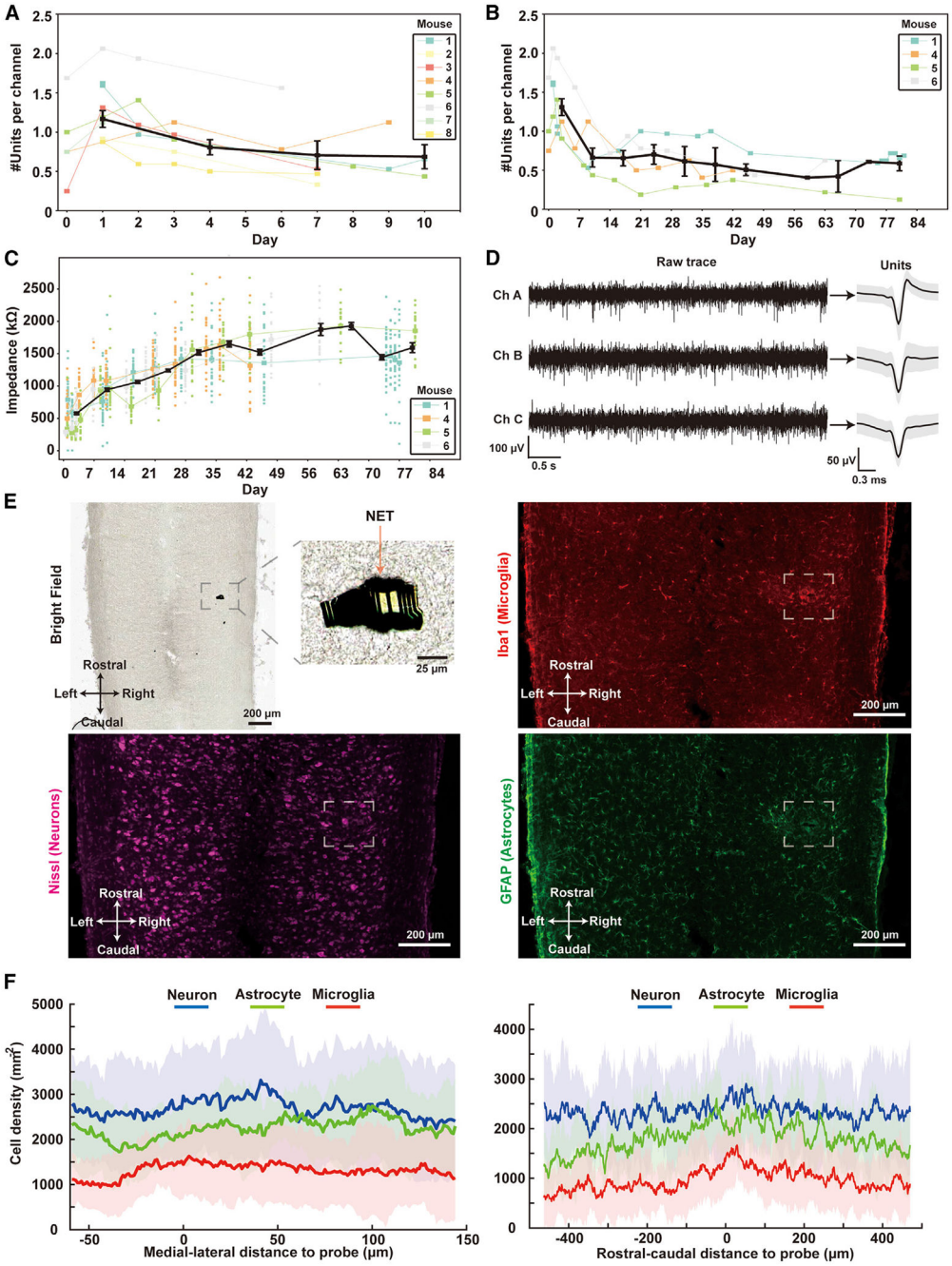

Figure 5. High-quality spikes and scarless tissue integration for months-long implantation

(A and B) Single unit yield per channel within 10 days post implantation for $n = 8$ mice (A) and within 84 days for a subset of $n = 4$ mice (B). Black curves show the average and error bars present the standard error. Individual animal's data are color coded.

(C) Impedance at 1 kHz within 84 days post implantation for the same animals ($n = 4$) in (B). Error bars present the standard error.

(D) Representative recording raw traces (left) and the spike waveform (right, shade presents SD) from three channels at 160 days post implantation.

Author Manuscript Author Manuscript Author Manuscript Author Manuscript

(E) Bright-field and immunofluorescence images of spinal cord tissue slice oriented with NET embedded. The tissue slice is perpendicular to the insertion direction of NET. The dashed rectangle refers to the implantation site. The black traces and black circles on the probe are the NET's conductive trace lines and electrode contacts, respectively.
(F) Spatial distribution of cell density (mean ± SD, shade presents SD) along the medial-lateral and rostral-caudal directions, respectively. NET implantation site is at 0 μm in both cases.

Author Manuscript Author Manuscript Author Manuscript Author Manuscript

KEY RESOURCES TABLE

REAGENT or RESOURCE	SOURCE	IDENTIFIER
Antibodies		
mouse anti-GFAP, 1:250	Millipore	Cat# MAB3402; RRID: AB_94844
rabbit anti-Iba1, 1:200	Fujifilm	Cat# 019–19741; RRID: AB_839504
NeuroTrace 640/660, 1:200	Invitrogen	Cat# N21483
donkey anti-mouse 488, 1:100	Invitrogen	Cat# A-21202; RRID: AB_141607
donkey anti-rabbit 594, 1:100	Invitrogen	Cat# A-21207; RRID: AB_141637
Experimental models: Organisms/strains		
Mouse: C57BL6J	Jackson Laboratory	JAX: 000664
Software and algorithms		
MATLAB	MathWorks	R2021b
Intan RHX Data Acquisition Software	Intan	https://intantech.com/RHX_software.html
Open Ephys GUI	Open Ephys	https://open-ephys.org/gui
Uniform Manifold Approximation and Projection (UMAP)	UMA	https://umap-learn.readthedocs.io/en/latest/
MountainSort	MountainSort	https://github.com/flatironinstitute/mountainsort_examples/blob/master/README.md
CellExplorer	CellExplorer	https://cellexplorer.org/
DeepLabCut	DeepLabCut	https://www.mackenziemathislab.org/deeplabcut#:~:text=DeepLabCut%E2%84%A2%20is%20an%20efficient,typically%2050%2D200%20frames)).
Chronux toolbox	Chronux	http://chronux.org/
Mutual-Nearest-Neighbor algorithm	Chung et al.[60]	https://doi.org/10.1016/j.neuron.2018.11.002.
Estimation of unit locations	Boussard et al.[59]	N/A
QuPath	QuPath	https://qupath.github.io/
Original code for data processing	This paper	Zenodo: https://doi.org/10.5281/zenodo.10982225